

THREE-DIMENSIONAL SPHERICAL SIMULATIONS OF SOLAR CONVECTION. I. DIFFERENTIAL ROTATION AND PATTERN EVOLUTION ACHIEVED WITH LAMINAR AND TURBULENT STATES

MARK S. MIESCH,^{1,2} JULIAN R. ELLIOTT,² JURI TOOMRE,² TOM L. CLUNE,^{2,3}
 GARY A. GLATZMAIER,⁴ AND PETER A. GILMAN⁵

Received 1999 June 18; accepted 1999 October 26

ABSTRACT

Rotationally constrained convection possesses velocity correlations that transport momentum and drive mean flows such as differential rotation. The nature of this transport can be very complex in turbulent flow regimes, where large-scale, coherent vorticity structures and mean flows can be established by smaller scale turbulence through inverse cascades. The dynamics of the highly turbulent solar convection zone therefore may be quite different than in early global-scale numerical models, which were limited by computational resources to nearly laminar flows. Recent progress in high-performance computing technology and ongoing helioseismic investigations of the dynamics of the solar interior have motivated us to develop more sophisticated numerical models of global-scale solar convection. Here we report three-dimensional simulations of compressible, penetrative convection in rotating spherical shells in both laminar and turbulent parameter regimes. The convective structure in the laminar case is dominated by “banana cells,” but the turbulent case is much more complex, with an intricate, rapidly evolving downflow network in the upper convection zone and an intermittent, plume-dominated structure in the lower convection zone and overshoot region. Convective patterns generally propagate prograde at low latitudes and retrograde at high latitudes relative to the local rotation. The differential rotation profiles show some similarity with helioseismic determinations of the solar rotation but still exhibit significantly more cylindrical alignment. Strong, intermittent, vortical downflow lanes and plumes play an important dynamical role in turbulent flow regimes and are responsible for significant differences relative to laminar flows with regard to momentum and energy transport and to the structure of the overshoot region at the base of the convection zone.

Subject headings: convection — hydrodynamics — stars: interiors — Sun: interior — Sun: rotation — turbulence

1. INTRODUCTION

Convection in the Sun is highly turbulent. The molecular viscosity is very small relative to the amplitude and scale of the convective motions, and this gives very high characteristic Reynolds numbers—of order 10^{12} or more. We should therefore expect that large-scale convection below the photosphere is very vigorous, complex, and chaotic. In light of this, it is remarkable that some phenomena thought to be directly related to the dynamics of the convection zone exhibit a high degree of regularity. The most compelling of these are the 22 yr magnetic activity cycle and the apparently well-ordered, persistent differential rotation profile.

Many attempts to understand these and other features of global-scale solar convection from a theoretical point of view rely on highly simplified statistical parameterizations of convective turbulence, often based on some form of mixing-length or mean-field theory. Such parameterizations require assumptions about scale separation and homogeneity that may not accurately reflect the turbulent

dynamics. Recent simulations of compressible, rotating thermal convection in Cartesian geometries by Brummell, Hurlburt, & Toomre (1996, 1998) have revealed that many of the nonlinear correlations in turbulent parameter regimes are dominated by isolated, intermittent but spatially coherent, vortical downflows that are roughly aligned with the rotation axis and are associated with larger scale convection patterns near the top of the computational domain. Such structures arise from the coupling of turbulence with rotation and significantly influence the energy and momentum transport, thus giving rise to different mean flows and flux balance relative to comparable simulations of laminar convection. More generally, coherent structures and ordered flow components occur in a wide variety of turbulent systems, coexisting and interacting with more stochastic components (e.g., Cantwell 1981; Lumley 1991). The nature of this interaction and the role of coherent flow components may not be amenable to simple statistical parameterizations. The situation is further complicated by results from laboratory experiments of the highly turbulent Rayleigh-Bernard convection, which indicate two distinct regimes of turbulence distinguished by a different scaling of the heat flux with Rayleigh number and qualitatively different statistical properties (Heslot, Castaing, & Libchaber 1987; Kadanoff 1991). The high-Rayleigh-number “hard turbulence” seems to be associated with enhanced mixing zones adjacent to the boundary layers, driven by irregular, episodic thermal plumes.

To improve our understanding of solar convection, particularly with regard to mean flows, turbulent transport,

¹ Department of Applied Mathematics and Theoretical Physics, University of Cambridge, Silver Street, Cambridge CB3 9EW, England, United Kingdom; M.S.Miesch@damtp.cam.ac.uk.

² Joint Institute for Laboratory Astrophysics, University of Colorado, Boulder, CO 80309-0440.

³ SGI NASA Goddard Space Flight Center, Code 931, Greenbelt, MD 20771.

⁴ Earth Sciences Department, Earth and Marine Science Building, University of California, Santa Cruz, Santa Cruz, CA 95064.

⁵ High Altitude Observatory, National Center for Atmospheric Research, Boulder, CO 80307. NCAR is sponsored by the National Science Foundation.

and hydromagnetic dynamo action, numerical models must explicitly resolve and compute the nonlinear interactions among a large spectrum of convective modes. In addition, the coupling of the convection zone to the radiative interior by penetrative convection may be crucial to our understanding of the solar differential rotation and the solar dynamo. However, there is currently a lack of numerical models which incorporate three-dimensional turbulence, spherical geometry, rotation, convective penetration, and density stratification. Because of the large computational requirements for such models, they have become possible only recently with the advent of sufficiently powerful supercomputers. As high-performance computing technology continues to improve, numerical models promise to play an increasingly important role in our understanding of solar and stellar convection.

The need for improved numerical models of global solar convection is further emphasized by recent results from helioseismology, which have provided unprecedented information on the dynamics of the solar interior. In particular, helioseismology has made it possible to infer the variation of the solar angular velocity with latitude and radius, and the results are at variance with earlier numerical simulations of convection in fluid shells (e.g., Gilman 1977, 1979; Glatzmaier 1984, 1987; Gilman & Miller 1986). These simulations tend to produce angular velocity contours parallel to the rotation axis, while the helioseismic results indicate less cylindrical alignment, with contours parallel to radial lines at midlatitudes (Thompson et al. 1996; Schou et al. 1998). We expect that this discrepancy may be attributed to dynamics not fully captured by the simulations, involving momentum and energy transport associated with turbulent flow structures that must be explicitly computed and fully resolved. Angular momentum coupling between the convection zone and radiative interior through convective penetration may also play a role.

We have developed a numerical model of solar convection capable of addressing these issues. It is fully three-dimensional, and it incorporates a rotating spherical shell geometry with density stratification and convective penetration into an underlying stable region. The numerical algorithm has been designed specifically for optimal performance on the highest performance class of supercomputers available currently and for the foreseeable future, namely, scalably parallel architectures, otherwise known as massively parallel processor (MPP) systems. This allows us to achieve higher resolution and, consequently, more vigorous, turbulent flow regimes than previously achieved by other authors.

The details of the numerical model and our parallel implementation have been reported elsewhere (Clune et al. 1999). Elliott et al. (1999) gave a first account of some of the properties of our solar convection simulations in turbulent flow regimes. Other turbulent and laminar simulations have been examined by Elliott, Miesch, & Toomre (2000) with an emphasis on the influence of thermal boundary conditions on the angular momentum and energy balance and on the resulting differential rotation. This paper further investigates the nature of turbulent convection and its coupling with rotation by comparing in detail two simulations with very different Rayleigh numbers. The first of these exhibits laminar convective structures much like those found in earlier simulations of spherical-shell convection by other authors while the second is substantially more turbulent,

with a much more intricate, time-dependent flow structure. Unlike the previous studies of Elliott et al. (1999) and Elliott, Miesch, & Toomre (2000), both simulations presented here include convective penetration into an underlying region of stable stratification. The extent and character of this convective penetration are found to differ substantially between the laminar and turbulent flow regimes.

Section 2 provides a brief overview of the physical model, the governing equations, and the numerical method used to solve them, and in § 3 we review the parameter values used and other aspects of the simulations presented. The three-dimensional structure of the convection and the evolution and propagation of convective patterns is described in § 4. In § 5 we discuss the differential rotation and meridional circulation in each simulation, along with the latitudinal variation of the mean entropy and temperature profiles. Convective heat transport and energy flux balance are addressed in § 6. Throughout the paper, we emphasize the nature and dynamical influence of strong, intermittent, coherent downflows in turbulent parameter regimes, and § 7 is devoted to a more detailed discussion of this issue. The concluding section, § 8, is a summary. A more thorough study of the nonlinear momentum and energy transport in these simulations, as well as other aspects of the differential rotation maintenance, will be presented in another paper (Miesch, Elliott, & Toomre 1999, hereafter Paper II).

2. THE PHYSICAL AND NUMERICAL APPROACH

We numerically model thermal convection in a rotating spherical fluid shell under the anelastic approximation, which allows for a density contrast across the convection zone but effectively filters out high-frequency sound waves that would otherwise impose severe constraints on the magnitude of the time step needed to achieve numerical stability. The governing equations and solution method are very similar to those developed and applied to solar convection by Glatzmaier (1984, 1985a, 1985b). The primary difference in our model relative to Glatzmaier's is our numerical implementation, which is highly optimized for MPP computer architectures. This has allowed us to achieve much higher spatial resolution and, consequently, more turbulent parameter regimes by taking full advantage of recent progress in high-performance computing technology.

The anelastic equations of motion in the form used here were developed by Gilman & Glatzmaier (1981; see also Glatzmaier 1984, Miesch 1998, Clune et al. 1999). They are fully nonlinear in velocity variables and linearized in thermodynamic variables with respect to a spherically symmetric mean state having a density, temperature, pressure, and specific entropy of $\bar{\rho}$, \bar{T} , \bar{P} , and \bar{S} . Perturbations about this mean state are denoted by ρ , T , P , and S . To lowest order, the fluid velocity \mathbf{v} has no spherically symmetric component ($\bar{v} = 0$). The mean state is periodically updated with the spherically symmetric component of the thermodynamic perturbations and therefore evolves as the convection modifies the stratification, particularly in the overshoot region, and establishes a statistically steady state.

The governing equations include the mass continuity equation,

$$\nabla \cdot (\bar{\rho} \mathbf{v}) = 0, \quad (1)$$

the momentum equation,

$$\bar{\rho} \frac{\partial \mathbf{v}}{\partial t} = -\bar{\rho}(\mathbf{v} \cdot \nabla) \mathbf{v} - \nabla P - \nabla \cdot \mathcal{D} + \rho \mathbf{g} + 2\bar{\rho}(\mathbf{v} \times \boldsymbol{\Omega}) - [\nabla \bar{P} - \bar{\rho} \mathbf{g}], \quad (2)$$

the internal energy equation,

$$\bar{\rho} \bar{T} \frac{\partial S}{\partial t} = \nabla \cdot [\kappa \bar{\rho} \bar{T} \nabla (\bar{S} + S) + \kappa_r \bar{\rho} C_p \nabla (\bar{T} + T)] - \bar{\rho} \bar{T} \mathbf{v} \cdot \nabla (\bar{S} + S) + 2\nu \bar{\rho} [e_{ij} e_{ij} - \frac{1}{3}(\nabla \cdot \mathbf{v})^2], \quad (3)$$

and the equation of state

$$\frac{\rho}{\bar{\rho}} = \frac{P}{\bar{P}} - \frac{T}{\bar{T}} = \frac{P}{\gamma \bar{P}} - \frac{S}{C_p}. \quad (4)$$

The viscous stress tensor is given by

$$\mathcal{D}_{ij} = -2\bar{\rho} \nu [e_{ij} - \frac{1}{3}(\nabla \cdot \mathbf{v}) \delta_{ij}], \quad (5)$$

and an ideal gas is assumed:

$$\bar{P} = \mathcal{R} \bar{\rho} \bar{T}. \quad (6)$$

The symbols $\boldsymbol{\Omega}$, \mathcal{R} , \mathbf{g} , C_p , e_{ij} , and γ denote the rotation rate of the coordinate system, the gas constant, the gravitational acceleration, the pressure-specific heat, the strain rate tensor, and the ratio of specific heats (C_p/C_v) respectively. The boundary conditions used in the present study are impenetrable and stress-free, with a fixed entropy gradient imposed on the bottom surface and a fixed entropy imposed on the top. The bracketed term in equation (2), $\nabla \bar{P} - \bar{\rho} \mathbf{g}$, vanishes initially because the mean state begins in hydrostatic balance. However, as the convection becomes established, this term becomes nonzero because of the influence of what can be regarded as a turbulent pressure. The radiative diffusivity, κ_r , is a function of radius alone and is based on results from solar structure models. It is this radiative diffusion term that accounts for all the stellar luminosity deep in the underlying convectively stable region (see § 6).

The diffusive transport coefficients ν and κ are also assumed to be dependent on the radius alone. Ideally, they would represent molecular diffusion processes, but a numerical model that explicitly resolves the full range from global scales in the Sun to molecular diffusion scales is unattainable now and for the foreseeable future because of the enormous computational requirements. The coefficients ν and κ should therefore be regarded as an effective eddy viscosity and eddy diffusivity, arising from momentum and heat transport by turbulent motions on scales smaller than the spatial resolution of the model. In this sense, our model is a large eddy simulation (LES) with parameterizations for sub-grid-scale (SGS) transport.

The functional form of SGS parameterizations in general may be specified or determined from properties of the large-scale flow according to one of many prescriptions (e.g., Lesieur 1990; Canuto 1997) and may involve higher order powers of ∇^2 , known as hyperviscosity, in order to limit the influence of diffusion on the resolved motions. Our model can also be configured to admit some more sophisticated prescriptions that arise from a formal LES-SGS filtering procedure and make use of various turbulence closure models (e.g., Lesieur 1990; Xie & Toomre 1993; Canuto & Christensen-Dalsgaard 1998), although some of the dynamic versions of SGS (e.g., Germano et al. 1991) may be

difficult to implement. In the simulations reported here, we use a crude functional form for ν and κ , $\propto \bar{\rho}^{-1/2}$ (see § 3), which behaves as a ∇^4 hyperviscosity for the highest spherical harmonic modes. The belief is that at some level of resolution the global-scale dynamics will become insensitive to details of dissipation and SGS transport, a conjecture which seems to be valid at least in systems that are not sensitive to boundary effects (Mason 1994). Since buoyancy driving for global-scale solar convection occurs in regions of finite extent, determined by the mean stratification and independent of dissipation, boundary effects of this type should not limit the applicability of the LES-SGS approach as long as these regions are resolved. This is in contrast to, e.g., turbulent Rayleigh-Bernard convection, where buoyancy driving occurs in thermal boundary layers that become narrower as the dissipation is decreased (e.g., Siggia 1994) and LES-SGS treatments are generally unreliable.

The anelastic approximation implicit in equations (1)–(6) is valid as long as typical flow velocities remain substantially subsonic and the stratification does not become appreciably superadiabatic. According to solar structure models (J. Christensen-Dalsgaard, 1999, private communication), departures from the adiabatic temperature gradient greater than 1% are confined to the upper 1000 km of the convection zone, which lies outside of our computational domain (see § 3).

The equations are solved in a rotating spherical shell using a pseudo-spectral method. Truncated expansions in terms of spherical harmonic and Chebyshev basis functions are used for the horizontal and radial dimensions respectively. Temporal discretization is accomplished using a semi-implicit Crank-Nicholson time-stepping scheme for the diffusive, pressure-gradient, and buoyancy terms and an explicit Adams-Bashforth scheme for the nonlinear and Coriolis terms. The mass flux, $\bar{\rho} \mathbf{v}$ is represented in terms of stream functions in order to ensure that the mass continuity equation (1) is satisfied identically throughout the simulation. The radial discretization can optionally include either one or two separate *stacked* Chebyshev expansion domains. The stacked Chebyshev option is used in the simulations presented here in order to provide enhanced resolution in the overshoot region near the base of the convection zone. Supplemental equations ensure the continuity of velocity, thermodynamic variables, conductive heat flux, and fluid stresses across Chebyshev domains.

The numerical algorithm has been specifically designed to run highly efficiently on MPP architectures. A message-passing communication strategy is used that is based on the MPI (message passing interface) standard. To enhance efficiency on Cray platforms, some of the key MPI routines have been replaced by analogous routines from the vendor-supplied SHMEM communication library. All spectral transformations are applied to data local to each processor, with interprocessor transposes performed when necessary to arrange for the transformation dimension to be local. Since this approach minimizes the communication volume, it is more efficient than parallel transformation algorithms when the problem size and the number of processors is large (Foster & Worley 1997). Data is distributed in several different configurations with the intention of achieving optimal load-balancing and to minimize the required number of interprocessor transposes. The triangular nature of the spherical harmonic data structures makes such load-balancing nontrivial, and a somewhat sophisticated algo-

rithm has been implemented to optimize the data partitioning. Because there is no “fast” algorithm available analogous to an FFT, the Legendre transformations dominate the workload as the problem size becomes large. As a result, much effort has been taken to highly optimize them, and near peak performance has been achieved on cache-based architectures by exploiting equatorial symmetries of the associated Legendre functions, structuring arrays and loops to operate on blocks that efficiently fit into on-chip cache, and reusing arrays in cache as often as possible to minimize cache misses. Dynamic memory management is used throughout the code to provide efficiency and clarity. Also, vendor-supplied FFT, cosine transform, and matrix-solution routines are used to maximize efficiency while employing standard interfaces to retain portability.

The code has been running in production mode for approximately two years, first on the 256 node IBM SP2 at the Cornell Theory Center (CTC), and later on the 512 node Cray T3E at the Pittsburgh Supercomputing Center (PSC). Current production platforms include the Cray T3E machines at the NASA Center for Computational Sciences (NCCS) and the San Diego Supercomputing Center (SDSC), as well as the SGI/Cray Origin 2000 at the National Center for Supercomputing Applications (NCSA). Sustained speeds of up to 160 Mflops per node have been demonstrated on the NCCS T3E with good scalability (Clune et al. 1999).

3. SIMULATION SETUP AND PARAMETER VALUES

The primary goal of this paper is to investigate the role of turbulence in rotating spherical-shell convection. We report the results of two simulations, summarized in Table 1, which have very different levels of buoyancy driving relative to SGS-eddy dissipation but are similar in other respects,

such as geometry, rotation rate, and boundary conditions. They have been labeled LAM and TUR, in light of their relatively laminar and turbulent nature. Note that the governing equations (1)–(6) are dimensional, so the non-dimensional parameters listed in Table 1 are computed a posteriori.

The rotation rate of the coordinate system, Ω , is taken to be $2.6 \times 10^{-6} \text{ s}^{-1}$ in both simulations, corresponding to a rotation period of about 28 days, which is the observed rotation period of the solar surface at midlatitudes. The computational domain extends from $0.62 R_\odot$ to $0.96 R_\odot$, and the initial stratification is based on a standard one-dimensional solar structure model (Elliott 1998). The luminosity carried by the model is approximately equal to the solar luminosity throughout the computational domain (see Fig. 18).

Our domain does not extend to the photosphere because the vigorous, highly compressible, granular convection and the strongly superadiabatic stratification in the solar surface layers impose restrictive spatial and temporal resolution requirements and lead to a breakdown in the anelastic approximation. It is uncertain what effect, if any, these surface layers have on the deep, global-scale convection we are modeling. Boundary layers play a crucial role in solar granulation (e.g., Stein & Nordlund 1998) and in turbulent Rayleigh-Bernard convection (e.g., Siggia 1994), but deep solar convection is not sensitive to the radiative transfer effects that dominate in the former case and, as mentioned in § 2, the buoyancy driving occurs in regions that remain of finite extent in the dissipationless limit, unlike the latter case. We may therefore expect that deep solar convection is insensitive to what occurs very near the photosphere.

Resolution limitations also preclude a direct simulation of the sharp transition from subadiabatic to superadiabatic

TABLE 1
SIMULATION PARAMETERS

Parameter	Notation	LAM	TUR
Resolution	$N_r, N_\theta, N_\phi (T\ell_{max})$	98, 64, 128 (T42)	98, 256, 512 (T170)
Top Eddy Viscosity ^a	$\nu(r_o)$	1.9×10^{13}	3.0×10^{12}
Rayleigh Number ^{b,c} (R_a)	$(-\partial\rho/\partial S)\Delta Sgd^3$	6.2×10^3	9.8×10^4
	$\rho\nu\kappa$		
Critical Rayleigh Number ^b	R_{ac}	1159	984
Supercriticality	$\frac{R_a}{R_{ac}}$	5.4	100
	R_{ac}		
Taylor Number ^{b,c} (T_a)	$\frac{4\Omega^2 d^4}{\nu^2}$	2.5×10^4	1.0×10^6
	$\frac{\nu}{\kappa}$		
Prandtl Number (P_r)	$\frac{\nu}{\kappa}$	0.1	0.1
Outer Boundary	r_o	$0.96 R_\odot$	$0.96 R_\odot$
Inner Boundary	r_i	$0.62 R_\odot$	$0.62 R_\odot$
Convection Zone Base	r_b	$0.75 R_\odot$	$0.76 R_\odot$
Density Contrast ^d	$\frac{\bar{\rho}(r_i)}{\bar{\rho}(r_o)} \left[\frac{\bar{\rho}(r_b)}{\bar{\rho}(r_o)} \right]$	54 [22]	53 [19]
Convective Rossby Number ^b	$\sqrt{\frac{R_a}{P_r T_a}}$	1.6	0.99
Rossby Number ^b (R_o)	$\frac{\omega_{rms}}{2\Omega}$	0.54	1.9

^a In both simulations, ν and κ are proportional to $\bar{\rho}^{-1/2}$.

^b Evaluated near the middle of the convection zone.

^c The length scale, d , used for these nondimensional quantities is 140 Mm, which is approximately the depth of the convection zone in each simulation.

^d The values without brackets correspond to the entire computational domain and those within square brackets to the convectively unstable portion alone.

stratification that occurs at the base of the solar convection zone. The magnitude of the subadiabatic entropy gradient in the radiative interior for our simulations is approximately 2 orders of magnitude larger than the superadiabatic entropy gradient in the mid convection zone (Fig. 1). For comparison, this ratio is about 5 orders of magnitude in the Sun according to standard structure models (e.g., Elliott 1998). The relatively weaker transition from superadiabatic to subadiabatic stratification in our simulations results in an overshoot region at the base of the convection zone that is wider than that which is thought to exist in the Sun. However, such an approximation is necessary in order for convective penetration to be adequately resolved.

Both simulations were initiated from the same laminar progenitor solution, similar in its parameter values and flow structure to case LAM. Starting from this common state, case LAM has evolved for over 1600 simulated days ($>200,000$ time steps) and case TUR for almost 1200 days ($>600,000$ time steps)—over 60 and 40 rotation periods, respectively. More precisely, simulation TUR went through an intermediate stage with a slightly higher viscosity and diffusivity [$\nu(r_0) = 5 \times 10^{12}$; $P_r = 0.1$], lasting about 700 days (300,000 iterations), and has been continued for another 490 days ($>300,000$ iterations) at its current parameter values (Table 1). The flow characteristics of this intermediate stage have been described by Miesch (1998) and are similar in many ways to the later, more turbulent stage presented here.

The common progenitor state for the two simulations exhibited a differential rotation similar to that in case LAM (see § 5.1). The question therefore arises as to whether the differential rotation in case TUR is to some extent a remnant of this initial state. The timescale for any initial differential rotation to dissipate by sub-grid-scale viscous diffusion alone is of order 100 yr, based on the eddy viscosity used in case TUR. This is much longer than the simulation duration of 1200 days, which is about 3 yr. However, in the presence of bulk convective motions and global-scale circulations, the spin-down timescale for the shell is much less—of the order of months. Therefore, the differential rotation in case TUR is not simply inertia from the laminar progenitor state. However, a strongly nonlinear dynamical system, such as case TUR, may exhibit more than one attractor in phase space, and the full time history

of the simulation could determine which basin of attraction the system falls in to.

An increase in the degree of turbulence is achieved by decreasing the eddy viscosity, ν , and the eddy diffusivity, κ , while holding the remaining input parameters constant. Both ν and κ are chosen to have the same radial profile, increasing with radius $\propto \bar{\rho}^{-1/2}$. This and similar radial profiles ($\nu, \kappa \propto \bar{\rho}^\alpha$ with $\alpha = 0, -\frac{1}{2}$, and -1) have been studied previously in the linear analysis of convective modes by Glatzmaier & Gilman (1981b) and in the nonlinear convection simulations of Gilman & Miller (1986). Although such profiles are crude, there is some justification because, according to mixing-length arguments, the energy-containing eddies should be larger in the lower convection zone as a result of the larger pressure scale height, so they should be better resolved by the numerical model and less remains to be parameterized (the horizontal grid spacing is somewhat smaller near the bottom of the computational domain as well). Furthermore, there is some question as to whether momentum transport by compressible SGS turbulence is better approximated by a constant kinematic viscosity (ν) or a constant dynamic viscosity ($\bar{\rho}\nu$). In any case, as mentioned in § 2, such SGS parameterizations should become irrelevant in the small dissipation limit, where the dynamics on large scales are essentially inviscid. As our simulations achieve more turbulent flow regimes, we come closer to this ideal, although in practice, we have not yet reached it fully. Other radial profiles for ν and κ have been considered by Elliott et al. (1999) and Elliott, Miesch, & Toomre (2000).

The SGS-eddy coefficients have been varied together such that their ratio, the Prandtl number (ν/κ), is constant throughout the shell and is the same in both simulations. We focus on the low Prandtl number regime ($P_r = 0.1$) in order to favor the vortex-stretching and shear instabilities that characterize three-dimensional turbulence and to emphasize the influence of Reynolds stresses for a given Rayleigh number. Note that the relative importance of inertial and viscous forces is related to the Grashof number, $G_r = R_a/P_r$ (e.g., Tritton 1988), so the simulations presented here are more turbulent than others in the literature that have comparable Rayleigh numbers but higher Prandtl numbers.

The Rayleigh number, R_a , provides a measure of the magnitude of buoyancy forces relative to viscous and thermal dissipation; we have defined it based on the total entropy change across the convection zone (Table 1). However, the buoyancy driving in general varies with depth, and the degree of convective instability depends on a number of factors, such as the rotation rate and the stratification. A better indication of the strength of the driving in each of the simulations can therefore be obtained by computing the global supercriticality, that is, the magnitude of the Rayleigh number relative to the critical Rayleigh number for the onset of convection. The critical Rayleigh number for each of the simulations was determined by introducing small perturbations to the mean spherically symmetric stratification and computing their time evolution according to the linearized versions of equations (1)–(6). By repeating this calculation for a series of ν and κ values (holding the Prandtl number constant), the perturbation growth rate can be plotted as a function of Rayleigh number. Interpolating this curve to zero growth rate gives the critical Rayleigh number. The critical Rayleigh numbers

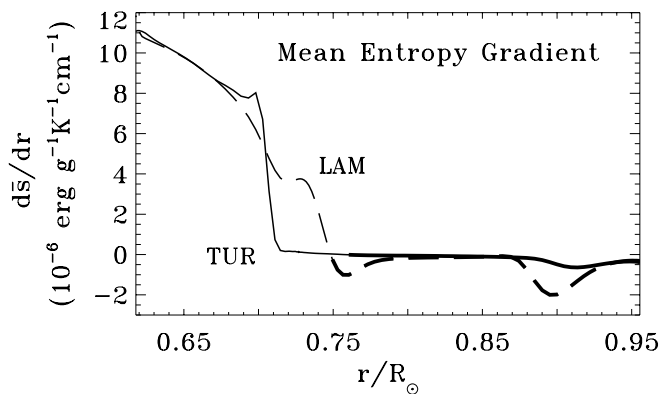


FIG. 1.—Spherically symmetric component of the entropy gradient, dS/dr , shown as a function of radius for both cases TUR (solid line) and LAM (dashed line). The convection zone, defined as the region of superadiabatic stratification ($dS/dr < 0$) is indicated in both cases with bold lines.

for the two simulations (Table 1) are slightly different because the convection in each case has modified the mean stratification, as demonstrated in Figure 1. As shown, the more efficient convection in the turbulent solution, TUR, has established a mean stratification that is more nearly adiabatic in the convection zone relative to the laminar solution, LAM. Furthermore, the region of convective penetration is deeper and more adiabatically stratified in case TUR. The supercriticality based on the evolved mean state for case TUR is 100, almost a factor of 20 larger than that for case LAM.

A decrease in the eddy viscosity ν yields not only a larger Rayleigh number and supercriticality but also a larger Taylor number (Table 1). Such a simultaneous increase in both the Rayleigh and Taylor numbers is desirable in light of the early Boussinesq results on convection in rotating spherical shells by Gilman (1977). He conducted a series of simulations with a constant Taylor number and found that as the Rayleigh number was progressively increased, the character of the convection changed dramatically, particularly with regard to the differential rotation profile. As the ratio of buoyancy forces to Coriolis forces, known as the *convective* Rossby number (see Table 1), became much larger than unity, the angular velocity profile completely reversed, from a prograde maxima at the equator near the upper boundary to a retrograde minima (in both cases the angular velocity contours were approximately aligned with the rotation axis). When buoyancy forces dominate over Coriolis forces, the convection tends to conserve angular momentum and spin down the low-latitude surface layers. This is in striking contrast to the surface angular velocity observed on the Sun, which decreases monotonically from equator to pole.

We wish to increase the vigor of the convection by reducing the dissipation, not by increasing the buoyancy driving. In particular, we want the relative magnitude of buoyancy forces and Coriolis forces to remain comparable as the flows become more turbulent, which requires a simultaneous increase in both the Rayleigh and Taylor numbers in such a way that the convective Rossby number remains of order unity. Since the code is dimensional, we achieve this by adjusting the magnitude of the SGS-eddy viscosity and diffusivity while keeping the remaining parameters constant, as mentioned above. The small reduction in the convective Rossby number in case TUR relative to case LAM arises solely from the feedback of convection on the mean stratification (which yields a change in ΔS).

Although the ratio of buoyancy to Coriolis forces remains comparable in cases LAM and TUR, the ratio of fluid vorticity to planetary vorticity is larger in the latter case. In other words, although the *convective* Rossby number in case TUR is comparable to that in case LAM, the more *standard* Rossby number, R_o , is significantly larger (Table 1). The latter number, R_o , reflects the relative importance of the advection and Coriolis terms in the vorticity equation and provides another measure of the rotational influence. In case LAM, R_o is less than unity throughout all but the uppermost convection zone, indicating that fluid motions are in general strongly influenced by rotation. By comparison, it exceeds unity throughout most of the convection zone in case TUR because of the presence of intense small-scale vorticity. The interaction between such a small-scale flow component and larger scale, more rotationally constrained motions may help to explain the departure of

the solar differential rotation profile from a cylindrically symmetric, Taylor-Proudman state (see § 5.1).

4. CONVECTION STRUCTURE AND TEMPORAL VARIATION

4.1. Three-Dimensional Morphology

The structure of the convection in case TUR is illustrated in Figure 2, which shows the radial velocity, temperature perturbation, and radial vorticity for three different horizontal levels at a particular instant in time. A similar representation of the convection structure in case LAM is exhibited in Figure 3.

It is evident from Figures 2 and 3 that the substantial difference in supercriticality between the two simulations produces a dramatic difference in the appearance of the convection. The complex morphology of case TUR bears little resemblance to the large-scale, columnar “banana-shaped” convection cells that dominate in case LAM and in previously published simulations of relatively laminar convection in rotating spherical shells (Gilman 1977, 1979; Glatzmaier 1984, 1987; Gilman & Miller 1986).

In the upper convection zone, case TUR exhibits an intricate network of narrow downflow lanes surrounding broader, weaker upflows (see Fig. 2, *upper panels*). Although well-defined periodic banana modes are absent, transient, isolated, latitudinally aligned downflow lanes often appear at low latitudes, typically lasting for days or weeks before they are advected and fragmented by horizontally diverging flows from newly established upwellings. The convection pattern at higher latitudes is generally more homogeneous and is associated with somewhat smaller spatial scales. Within the cellular network there occur a number of localized, strong upflows, each surrounded by a narrow downflow ring. An example is highlighted on the zoomed-in radial velocity image of Figure 2 (a second example is visible just below it). Such features occur particularly at high and mid latitudes, usually originating at the interstices of the downflow network. They arise from the combined effects of rotation and compressibility, particularly at low Prandtl number, and similar structures have been observed previously in three-dimensional simulations of turbulent convection in Cartesian geometries by Brummell, Hurlburt, & Toomre (1996) and Brandenburg et al. (1996). As downflows tend to compress because of the density stratification, Coriolis forces induce cyclonic vorticity, forming radially aligned vortex tubes. As in a cyclone, pressure gradients are established that tend to balance the Coriolis and centrifugal acceleration, which leads to an evacuation of the tube center. This effect is especially pronounced when the Prandtl number is low. Buoyancy forces accelerate the low-density core of the tube upward, thus reversing the downflow. Surrounding this upflowing core is a downflow ring associated with a vortex sheath (see Fig. 2). Eventually, the expansion of the upflowing core breaks up the surrounding downflow lane and produces a broad, warm upwelling that forms the center of a new convection cell. This destabilization of vortical downflows by “dynamical buoyancy” results in a continual destruction and regeneration of the cellular convection network near the top of the convection zone, accelerating and altering the time evolution relative to what it would be in the absence of rotation (Brummell et al. 1996). The structure and evolution of the cellular network in the upper convection zone of both simulations will be described in more detail in the following section (§ 4.2).

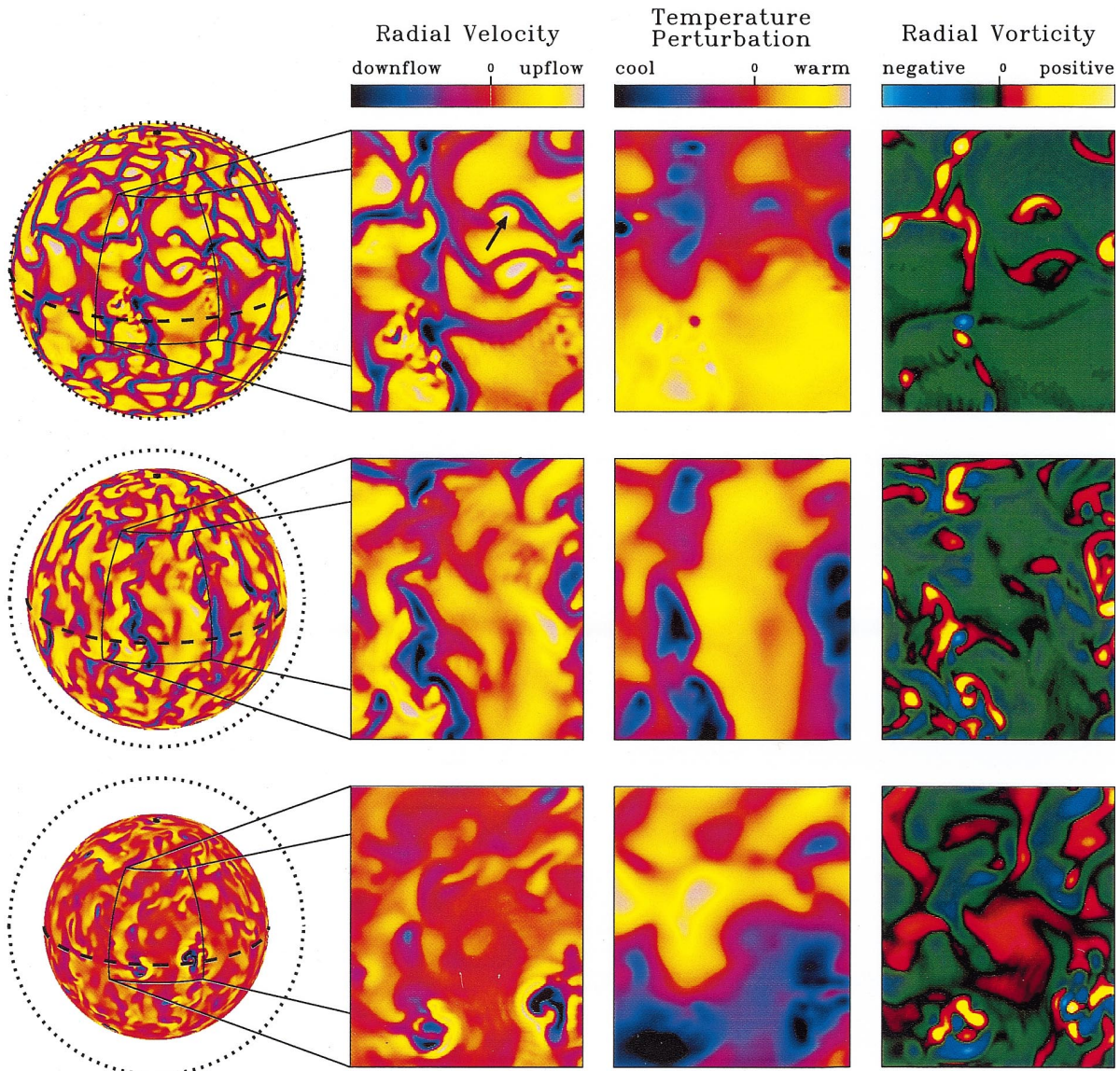


FIG. 2.—The left column shows instantaneous snapshots of the radial velocity on horizontal surfaces located in the upper convection zone (*top*), near the middle of the convection zone (*middle*), and in the overshoot region (*bottom*). In each image, the location of the outer boundary is indicated by a dotted line and the equator by a dashed line. The north pole in each surface, indicated by a black dot, is tilted 20° out of the paper. A blow-up of a $50^\circ \times 60^\circ$ segment in latitude and longitude is also shown at each level, as indicated by the solid lines. The arrow in the upper image highlights a vortical velocity feature discussed in the text. In the middle and right columns, the corresponding temperature perturbation and radial vorticity field are displayed. The color tables used for each of the three quantities are indicated, but the scaling varies with depth. In the northern hemisphere, positive and negative radial vorticity correspond to cyclonic and anticyclonic motions, respectively (vice versa in the southern hemisphere).

Deeper in the convection zone, the downflow network in case TUR is less well defined, although coherent, extended downflow lanes still exist (see Fig. 2, *middle left panel*). Outside these coherent downflow lanes, the surrounding velocity field is dominated by approximately uncorrelated, small-scale, turbulent fluctuations that become increasingly space-filling with increasing depth in the convection zone. Toward the bottom of the convection zone, the coherent downflows are generally less elongated horizontally and instead acquire a more plumelike character. The variation with depth of the convection structure in case TUR is generally comparable to that found in three-dimensional simulations of turbulent compressible convection in Cartesian geometries (Cattaneo et al. 1991; Brummell et al. 1996).

The plumelike nature of downflows in case TUR is especially apparent in the overshoot region, as shown in Figure

2 (*lower left-hand panel*). Strong, isolated, intermittent downflows penetrate deep into the stable zone, carrying low-entropy fluid and thereby establishing an approximately adiabatic stratification in the overshoot region (see Fig. 1). These overshooting plumes are generally connected to more extended downflow lanes at higher levels, forming coherent structures that often reach all the way up to the downflow network near the top of the convection zone. Coherent downflows extending from the upper convection zone deep into the overshoot region are often apparent in two-dimensional (r, ϕ) and (r, θ) cross sections of the instantaneous three-dimensional radial velocity and temperature fields (not shown).

In contrast, the convective patterns in case LAM are more periodic in longitude and exhibit much less small-scale structure (see Fig. 3). Persistent, regular banana modes

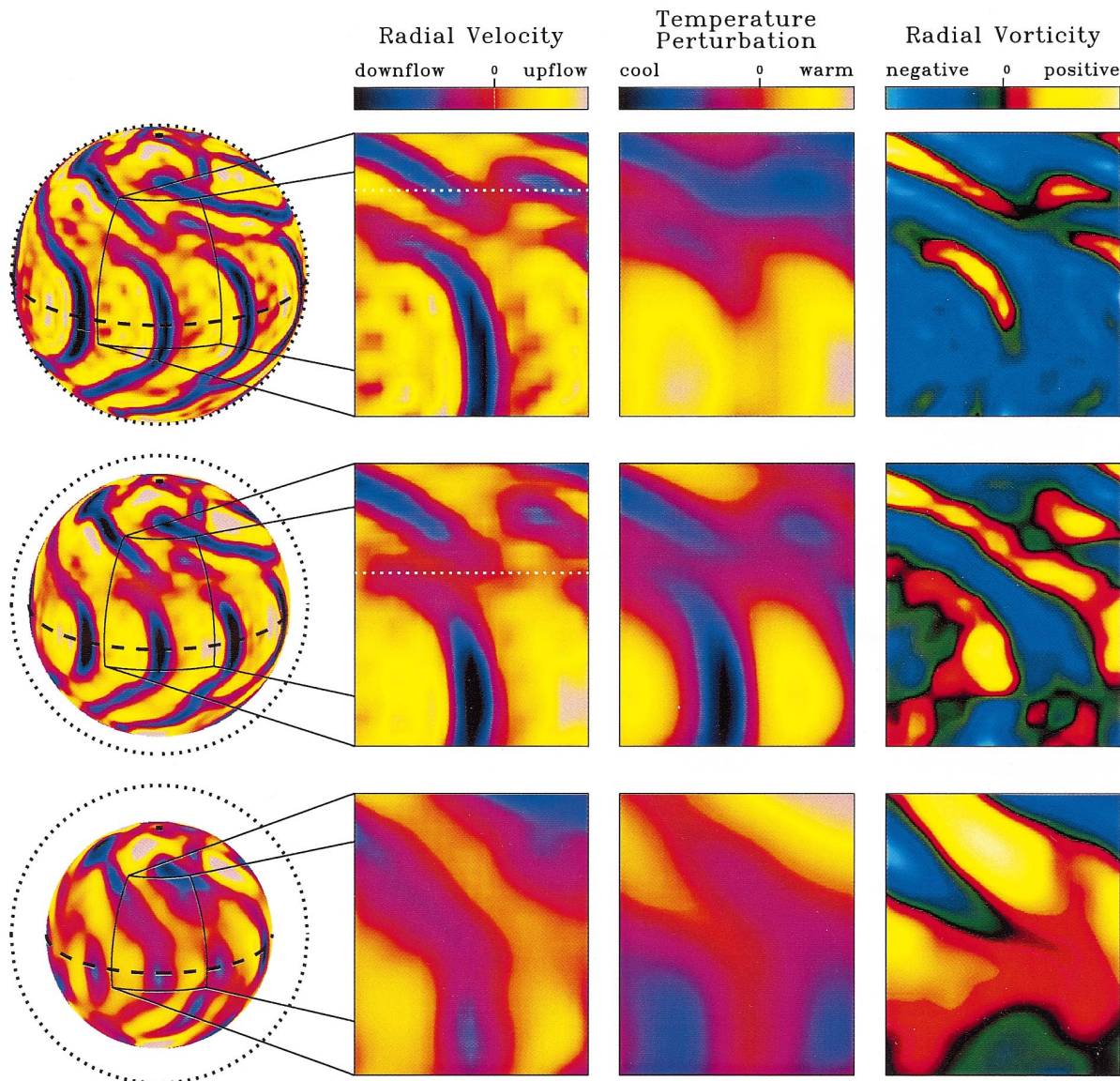


FIG. 3.—Similar to Fig. 2 but for case LAM. The white dotted lines in the upper and middle zoomed-in radial velocity images indicate the latitude corresponding to the cylinder tangent to the base of the convection zone and aligned with the rotation axis.

dominate at low latitudes, characterized by broad upflow lanes and narrow, stronger downflow lanes that are aligned with the rotation axis near the equator. At higher latitudes, there is a transition to more longitudinally elongated convection cells that continually break and recombine with the low-latitude banana modes (see § 4.2). As indicated by the white dotted lines in Figure 3, the latitude at which this transition occurs decreases with increasing depth in the convection zone and it coincides approximately with the cylinder tangent to the base of the convection zone and aligned with the rotation axis. In other words, this tangent cylinder marks the approximate dividing line between distinct equatorial and polar modes. This is a well known result that can be understood by studying the preferred linear modes for the onset of thermal convection in rotating spherical shells (e.g., Gilman 1975; Busse & Cuong 1977).

Apart from this change in the transitional latitude between equatorial and polar modes, there is little variation of the convective patterns in case LAM with depth. The dominant modes extend from the top to the bottom of the

convection zone and imprint themselves onto the overshoot region below, in sharp contrast to the intermittent plume structure of the overshoot in case TUR. Furthermore, the penetration in case LAM is shallower and less efficient, yielding a very different stratification near the base of the convection zone relative to case TUR (see Figs. 1 and 20).

In both simulations, strong downflows are well correlated with cooler temperatures. However, relative velocity-temperature correlations in weaker downflows and upflows are generally smaller in case TUR. This can be attributed primarily to the low Prandtl number, which implies that thermal diffusion is more efficient than momentum diffusion. As a result, temperature fluctuations are smoothed out relative to velocity fluctuations and they become less correlated on small scales.

The magnitude of the radial vorticity in both simulations tends to peak in downflow lanes, but this occurs to a much greater degree in the more turbulent case. The radial vorticity in particular for case TUR is strongly concentrated in isolated, plumelike downflows that often form in the upper

convection zone near the interstices of the downflow network. The highly vortical nature of these downflow regions is apparent in movies of the convection, which exhibit numerous “tornado-like swirls,” particularly at midlatitudes (one such swirl can be seen in Fig. 2, in the upper-middle portion of the blown-up region corresponding to the upper convection zone).

The sign of the radial vorticity is generally consistent with what is expected from the combined effects of Coriolis forces, density stratification, and spherical geometry (e.g., Yoshimura 1972; Gilman 1983; Glatzmaier 1985a, 1985b). In the bulk of the convection zone, downflows acquire a cyclonic radial vorticity component as they contract because of the stratification and geometry and subsequently “spin up” because of Coriolis forces. Similarly, expanding upflows acquire a Coriolis-induced anticyclonic vorticity component (“spin-down”). This gives rise to a negative (positive) helicity in the northern (southern) hemisphere throughout the upper and mid convection zones. Such a negative correlation between radial vorticity and radial velocity in the northern hemisphere is generally apparent in the upper and middle right-hand panels of Figures 2 and 3. However, it should be noted that case TUR also exhibits a number of paired cyclonic/anticyclonic vortices, often entirely within downflow lanes, which may be produced by the entrainment of surrounding material (see Fig. 2).

In the lower convection zone and overshoot region, the helicity reverses, caused primarily by the influence of diverging downflows that acquire anticyclonic vorticity as they expand (see Fig. 22). This effect is visible in the lower right-hand frames of Figures 2 and 3. However, note that the two most prominent downward plumes that appear in the overshoot region snapshots for case TUR (see Fig. 2, *lower panels*) both happen to occur near the equator, where the influence of Coriolis forces is weakest. They therefore exhibit more mixed helicity relative to comparable higher latitude plumes seen at other times in the simulation. Such strong, localized, high and mid latitude plumes possess a definite net helicity and give rise to a much more dramatic helicity reversal near the base of the convection zone in case TUR than in case LAM (see § 7).

4.2. Pattern Propagation and Evolution

A spectral decomposition of the velocity variance in terms of azimuthal wavenumber demonstrates more quantitatively the relatively wider distribution among contributing convective modes and scales in case TUR. Such a decomposition is shown in Figure 4 for three different horizontal levels in each simulation. In case LAM, there are prominent peaks at $m = 9$ and higher harmonics, reflecting the periodic, banana-type structure apparent in Figure 3. In contrast, the velocity spectra for case TUR are smoother, reflecting the stronger nonlinear coupling among modes. At intermediate wavenumbers, the spectra become somewhat steeper with increasing depth, but the downflow network near the top of the convection zone is associated with an increase in power at low wavenumbers relative to the mid convection zone, with a local peak at $m = 8$. Case LAM also exhibits a relative increase in power at low wavenumbers in the upper convection zone, but the effect is less pronounced. The spectrum in the overshoot region in this case is significantly steeper than in the convection zone.

Both simulations are well resolved throughout, with the velocity variance spanning at least 2–3 orders of magnitude

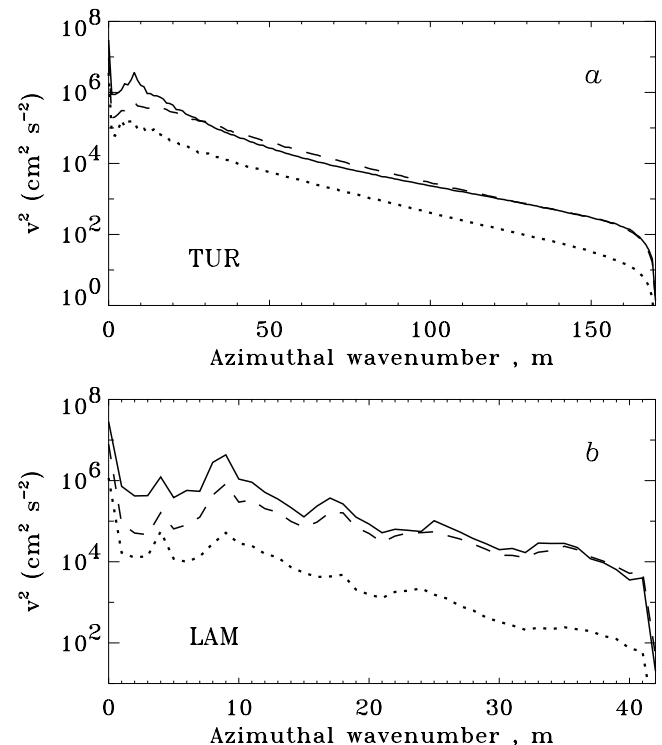


FIG. 4.—Azimuthal wavenumber spectra of the velocity squared is shown for (a) case TUR and (b) case LAM. In each panel, solid lines correspond to a horizontal level near the top of the convection zone ($r = 0.95 R_{\odot}$), dashed lines to a level in the mid convection zone ($r = 0.84 R_{\odot}$), and dotted lines to a level in the overshoot region ($r = 0.72 R_{\odot}$). All curves are averaged over a time interval of five rotation periods.

in spectral amplitude as a function of spherical harmonic degree and order (ℓ and m). The corresponding spectra of thermodynamic fluctuations, such as the variance of the temperature perturbation, are substantially steeper because of the low Prandtl number, spanning 4–6 orders of magnitude.

The peak in power at $m = 0$ for both simulations is primarily caused by the differential rotation, with a small contribution from the axisymmetric meridional circulation. In case TUR, the nonaxisymmetric ($m \neq 0$) convection modes account for about 75% of the total kinetic energy, with the differential rotation and meridional circulation contributing about 24% and 0.64%, respectively. In contrast, only about 60% of the total kinetic energy in case LAM is in nonaxisymmetric modes, with 38% in the differential rotation and 0.13% in the axisymmetric meridional circulation. The kinetic energy in the meridional circulation is typically 2%–4% of that in the differential rotation. In both simulations, temporal fluctuations in the nonaxisymmetric convection kinetic energy and in the differential rotation kinetic energy occur on timescales of weeks and months with amplitudes of 5%–10% relative to the mean. Temporal fluctuations in the meridional circulation kinetic energy are much greater, as large as 30%–45%.

An important question in the context of helioseismic and Doppler detection of large-scale velocity features on the Sun is how long such features last and, in particular, whether recognizable patterns persist over one or more rotation periods. The temporal variation of the horizontal radial velocity structure near the top of the convection zone

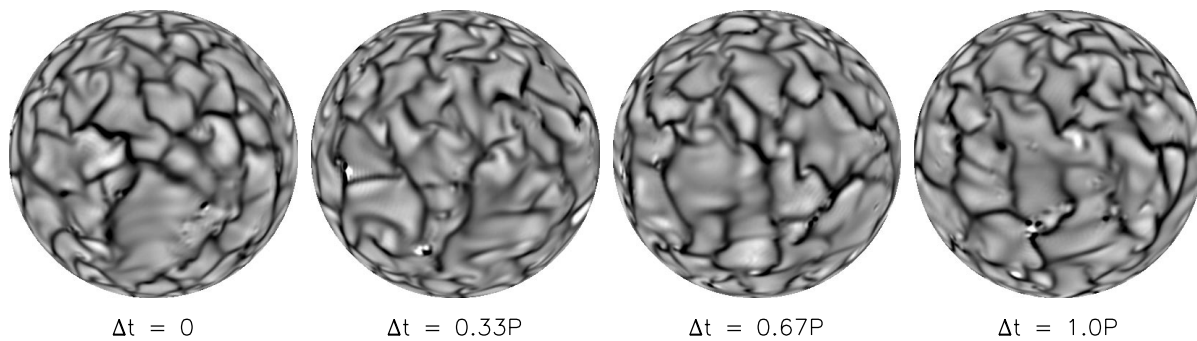


FIG. 5.—Snapshots of the radial velocity field in simulation TUR are shown at a level near the top of the convection zone ($r = 0.95 R_{\odot}$). The time interval between each successive image is about 9 days, one-third the rotation period of the coordinate system, P ($= 28$ days). Each surface is tilted 20° , such that the north pole points out of the plane of the page, as in Figs. 2 and 3. Light and dark regions denote upflow and downflow, respectively.

for each simulation is illustrated in Figures 5 and 6. Note that these snapshots are taken with respect to the rotating reference frame.

In case TUR, the convection structure is very time dependent, making it difficult to identify any persistent features over the course of a full rotation (28 days). As noted in § 4.1, strong downflow lanes aligned with the rotation axis often occur at low latitudes, but they typically persist only for days or weeks and are continually advected by horizontally diverging flows and differential rotation, making them difficult to track. The downflow network at the poles is generally more isotropic, is characterized by somewhat smaller spatial scales, and, again, evolves substantially on time-scales of weeks.

In contrast, the convection pattern in case LAM does not vary strongly with time. Banana modes persist for many rotation periods at low latitudes and propagate in a prograde direction (increasing longitude) relative to the rotating coordinate system at a rate faster than the local angular velocity of the fluid (see Table 2). A weak, smaller scale, more rapidly fluctuating flow component is also present near the outer boundary, visible in Figure 6 as a “cobbling” or “dimpling” superposed on the dominant banana structure (see also the upper images in Fig. 2). It is possible to track individual downflow lanes for many rotation periods, although snapshots such as those shown in Figure 6 often leave some ambiguity in discerning among similar features. Periodic, persistent modes also occur at midlatitudes, but their longitudinal propagation rate is slower, caused, in part, by the local differential rotation, and they continually break and recombine with the lower latitude banana modes. At high latitudes, low azimuthal wavenumbers dominate,

and they tend to propagate slowly retrograde. As mentioned in § 4.1, the transition between the low-latitude, rapidly propagating banana modes and the slower high-latitude modes occurs at a latitude that approximately coincides with the cylinder tangent to the base of the convection zone and aligned with the rotation axis. It is generally along or near this tangent cylinder where the breaking and recombining of low- and high-latitude modes occurs.

The longitudinal propagation and persistence of velocity features can be better demonstrated using images of the radial velocity field as a function of longitude and time, as displayed in Figures 7 and 8 for several chosen latitudes in the mid convection zone of each simulation. Each image spans the full 360° in longitude and covers a time interval of three rotation periods (84 days). A characteristic propagation speed for the patterns shown was obtained by first determining the predominant azimuthal wave mode at each latitude, defined as the wavenumber corresponding to the peak of the time-averaged Fourier spectrum in longitude. A Fourier transform in time was then used to compute a corresponding phase velocity for the predominant azimuthal mode at each latitude. The results are listed in Table 2.

In case TUR, the (ϕ, t) diagrams of Figure 7 reflect the complexity of the velocity field, suggesting the superposition of many coupled azimuthal modes propagating at different longitudinal phase speeds. New downflow lanes are being created and destroyed continually, and although few persist for the entire interval, many last longer than a rotation period, in contrast to the more rapidly evolving network near the surface. At low latitudes, most of the velocity features clearly propagate in a prograde direction relative to the rotating coordinate system but with varying

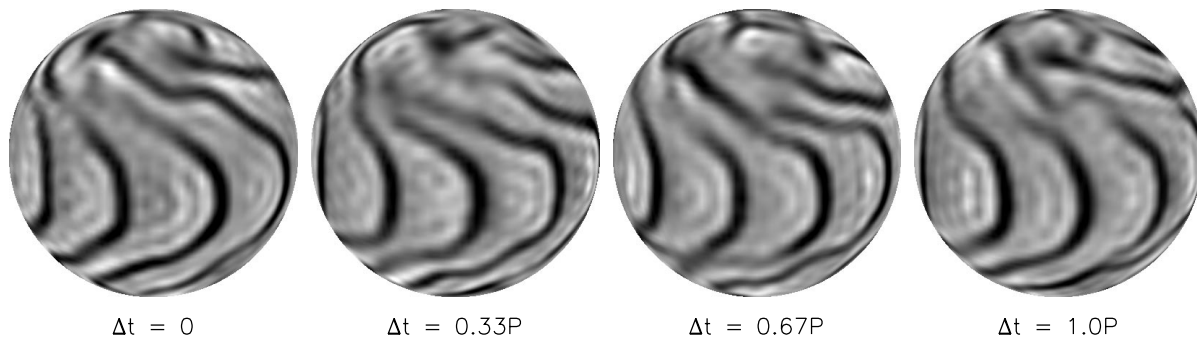


FIG. 6.—Similar to Fig. 5 but for case LAM

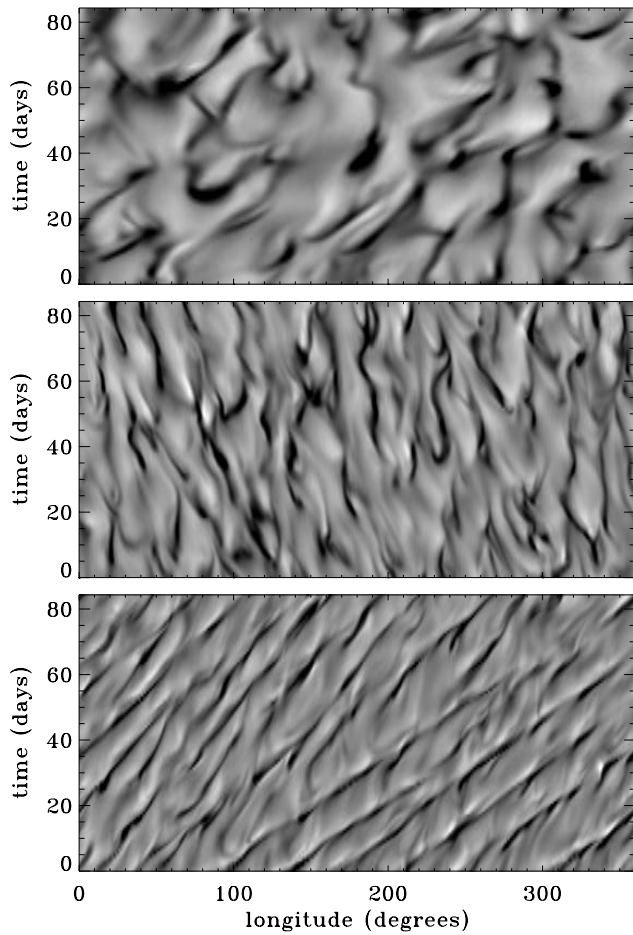


FIG. 7.—Shown is the radial velocity in the mid convection zone ($r = 0.84 R_{\odot}$) as a function of longitude and time at high, mid, and low latitudes. The upper image corresponds approximately to a latitude of 70° , the middle image to 40° , and the lower image to the equator (see Table 2).

speeds. In contrast, at midlatitudes, the (ϕ, t) pattern exhibits a leftward tilt, indicating retrograde propagation of velocity features relative to the rotating coordinate system. The top panel in Figure 7 reflects a shift in power toward lower azimuthal wavenumbers at high latitudes, although individual features tend to be localized, implying a significant contribution from higher harmonics.

The apparent shift toward lower wavenumbers at high latitudes is confirmed by the dominant azimuthal modes listed in Table 2, which reveal an $m = 7$ and an $m = 10$ response at high and low latitudes, respectively. At mid-latitudes the mean spectrum peaks at an even higher wave-

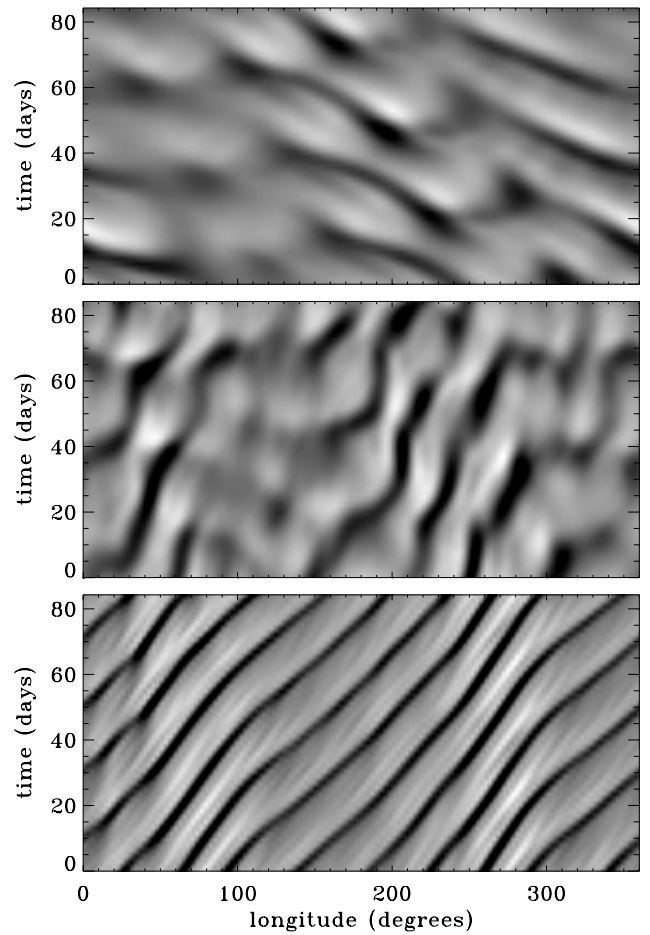


FIG. 8.—Similar to Fig. 7 but for case LAM. Again, upper, middle, and lower images correspond to latitudes of about 70° , 40° , and 0° , respectively (see Table 2).

number, $m = 16$, although many other modes are present as well. The characteristic phase speed of the low-latitude $m = 10$ mode indicates prograde propagation at a rate 23% faster than the rotating coordinate system (Table 2). Some of this rapid propagation is caused by advection by the local differential rotation, but when this contribution is subtracted out (Table 2), the result still indicates that the convection modes are propagating in a prograde direction faster than the local angular velocity at a rate of about 15% of the rotation rate of the coordinate system. At mid-latitudes, the dominant $m = 16$ mode is associated with a negative phase speed, indicating retrograde propagation relative to the rotating coordinate system. However, as

TABLE 2
PROPAGATION OF CONVECTIVE PATTERNS

Case	Latitude ($^{\circ}$)	Dominant Azimuthal Mode (m)	Longitudinal Phase Speed ^a ($\varpi \Omega^{-1}$)	Local Differential Rotation ^b $\langle v_{\phi} \rangle (r \sin \theta)^{-1} \Omega^{-1}$	Nonadvective Phase Speed $[\varpi - \langle v_{\phi} \rangle (r \sin \theta)^{-1}] \Omega^{-1}$
TUR	71	7	0.093	0.063	0.030
TUR	40	16	-0.021	-0.044	0.023
TUR	0.35	10	0.23	0.078	0.15
LAM	71	4	-0.33	-0.14	-0.19
LAM	40	8	0.082	-0.025	0.11
LAM	1.4	9	0.15	0.068	0.082

^a Relative to the rotating coordinate system: $\Omega = 2.6 \times 10^{-6} \text{ rad s}^{-1}$.

^b Averaged over longitude and over the three rotation time intervals used for Figs. 7 and 8.

shown in Table 2, this mode is actually propagating slowly in a prograde direction and is being advected backward by the local differential rotation. The high-latitude $m = 7$ mode is also propagating slowly prograde, boosted by the local differential rotation.

In case LAM, the persistence and propagation of banana modes is evident in the (ϕ, t) images of Figure 8, particularly at low latitudes. The mean azimuthal wavenumber spectrum of the low-latitude image exhibits a strong peak at $m = 9$, and this mode has a relatively well-defined prograde phase velocity that is faster than the local angular velocity (Table 2). In contrast, the dominant features at high latitudes are of significantly larger scale ($m \approx 4$) and propagate retrograde relative to the rotating coordinate system and relative to the local angular velocity. At midlatitudes, the pattern is more jumbled, with greater time dependence, more contributing azimuthal modes, and a phase velocity that is less well defined. Still, the analysis described above reveals a dominant, prograde-propagating $m = 8$ mode (Table 2).

We emphasize that the velocity features in Figures 5, 6, 7, and 8 are not simply advected along with the differential rotation. Rather, they represent traveling convective modes, each with a characteristic phase velocity. The propagation characteristics of the low-latitude modes are similar to the Rossby-like waves described by Glatzmaier & Gilman (1981a), which arise from the near-conservation of potential vorticity in the presence of a density stratification. For further results on the propagation of linear convective modes in rotating spherical shells, see Gilman (1975), Busse & Cuong (1977), Soward (1977), and Zhang (1994).

Persistent downflow lanes, such as those exhibited by both simulations LAM and TUR, are associated with horizontally converging flows in the upper convection zone and are therefore potential sites for the large-scale concentration of magnetic flux. Such structures may help to explain persistent regions of enhanced magnetic activity observed on the Sun and other stars, commonly referred to as “active longitudes” (e.g., Jetsu et al. 1997).

5. MEAN FLOWS AND THERMODYNAMIC VARIATIONS

5.1. Differential Rotation and Specific Entropy Profiles

It was mentioned in § 1 that thermal convection under the influence of rotation tends to redistribute angular

momentum and that this redistribution process is likely quite different in laminar and turbulent flow regimes. If the rotational influence is strong and baroclinic effects are weak, the resulting differential rotation profiles tend toward a Taylor-Proudman state in which angular velocity contours are parallel to the rotation axis. Previous simulations of solar convection in spherical shells generally gave angular velocity profiles of this type (Gilman 1977, 1979; Glatzmaier 1984, 1985a, 1987; Gilman & Miller 1986). Departures from such cylindrically aligned Taylor-Proudman states can occur because of baroclinicity (latitudinal entropy gradients) or flow components not strongly influenced by rotation, such as small-scale vortical motions that are part of a turbulent cascade.

Helioseismic results imply that the angular velocity profile in the highly turbulent solar convection zone is not cylindrically aligned (Thompson et al. 1996; Schou et al. 1998). Figure 9a illustrates the main features of the internal solar rotation profile as inferred from helioseismology, obtained from six months of p -mode frequency measurements by the GONG network of solar telescopes (Thompson et al. 1996; see also Fig. 11). Midlatitude angular velocity contours tend to be radially aligned rather than cylindrically aligned, and sharp radial gradients are confined to narrow shear layers near the base of the convection zone and just under the photosphere.

The lower shear layer is known as the solar tachocline and represents a narrow transition region between the differential rotation of the convection zone and the approximately solid body rotation of the radiative interior. Although the analysis is complicated by accuracy and resolution limitations in the helioseismic inversions, the tachocline seems to be centered at or slightly below the base of the convection zone, with a width $\lesssim 0.1 R_\odot$ and little latitudinal variation (Kosovichev 1996; Wilson, Burtonclay, & Li 1996; Basu 1997; Corbard et al. 1998; Antia, Basu, & Chitre 1998). Theoretical models suggest that intense horizontal turbulence and global-scale circulations driven by shear instabilities and magnetic effects produce poleward angular momentum transport in the tachocline and keep it relatively narrow (Spiegel & Zahn 1992; Elliott 1997; Gilman & Fox 1997; Gough & McIntyre 1998).

The upper shear layer near the surface is most pronounced at low latitudes. It is likely produced by the vigor-

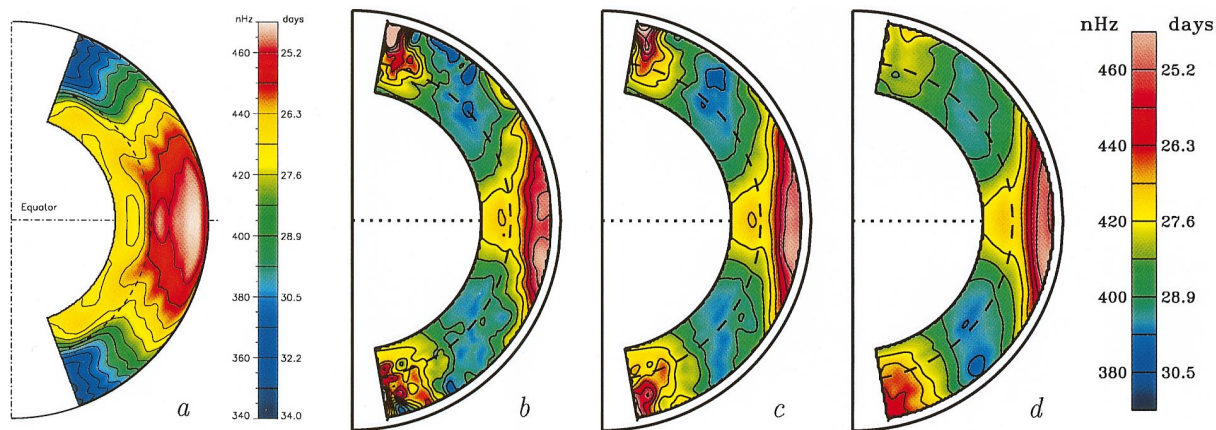


FIG. 9.—Longitudinally averaged angular velocity profiles: (a) the solar rotation according to an RLS inversion of p -mode frequency splittings from the first six months of GONG data (Thompson et al. 1996); (b)–(d) the rotation in simulation TUR; (b) at one time step; (c) averaged over one rotation period; and (d) averaged over 10 rotation periods. The color tables and contour levels used for the helioseismic and simulation data are indicated. Note that the computational domain does not extend all the way to the photosphere, as discussed in § 3.

ous small-scale convection observed in the photosphere as granulation, mesogranulation, and supergranulation. In contrast to the deep, global-scale convection studied here, this granular convection is highly compressible, less influenced by rotation and spherical geometry, more influenced by radiative transfer and ionization effects, and confined to the upper few percent of the Sun by radius. Computational limitations make it impractical to include such processes in our global-scale numerical simulations, although local numerical models of granulation by other authors have generally been quite successful in reproducing many aspects of solar observations (e.g., Stein & Nordlund 1998). Still, it is unclear how convection in the solar surface layers gives rise to the upper shear layer apparent in the helioseismic results of Figure 9a (see also Fig. 11b).

The solar differential rotation is remarkably smooth and steady. Photospheric measurements suggest that temporal variations in the surface rotation don't exceed a few percent, at least on timescales of years or less. However, there is evidence in both photospheric measurements and helioseismic inversions for weak ($\approx 5 \text{ m s}^{-1}$), small-scale ($\approx 10^\circ$ – 15° in latitude), torsional oscillations that originate at high latitudes, drift toward the equator in conjunction with the 22 yr activity cycle, and seem to be confined to the uppermost layers in the convection zone (Howard & LaBonte 1980; Kosovichev & Schou 1997; Schou et al. 1998). Reliable information on the temporal variability of the rotation in the deep solar interior currently awaits the acquisition and analysis of more high-quality helioseismic data from GONG and MDI/SOI.

Instantaneous and time-averaged angular velocity profiles for simulation TUR are shown in Figures 9b–9d. The instantaneous snapshot, Figure 9b, exhibits some small-scale fluctuations, but a smooth, large-scale component is apparent, with prograde rotation at low latitudes and retrograde rotation at midlatitudes relative to the rotating coordinate system, which has a period of 28 days. The polar regions generally exhibit prograde rotation as well, but they are more variable, both because of the smaller volume associated with the zonal average and because of the small-moment arm that translates small fluctuations in linear velocity into large-amplitude angular velocities (see Fig. 11a). Some residual small-scale structure remains in the one-rotation-period average profile (see Fig. 9c), but the ten-rotation-period average (see Fig. 9d) exhibits very little. Also, all three profiles, including the ten-rotation average, exhibit small but significant departures from equatorial symmetry. By construction, the helioseismic inversions only capture the equatorially symmetric component of the angular velocity profile (e.g., Thompson et al. 1996).

The rotation profiles in simulation LAM exhibit more equatorial symmetry and less small-scale structure and temporal variation (Fig. 10). As in case TUR, the angular velocity peaks near the equator toward the top of the computational domain and decreases with increasing latitude. However, case LAM does not exhibit a spin-up of the polar regions as in case TUR.

A “polar vortex” similar to that in case TUR was present in many previous simulations of solar convection in spherical fluid shells where it was attributed to the tendency of polar convective modes with low azimuthal wavenumber to conserve their angular momentum (Gilman 1977, 1979; Gilman & Miller 1986). The absence of a polar vortex in case LAM is caused, in part, by the equatorward transport

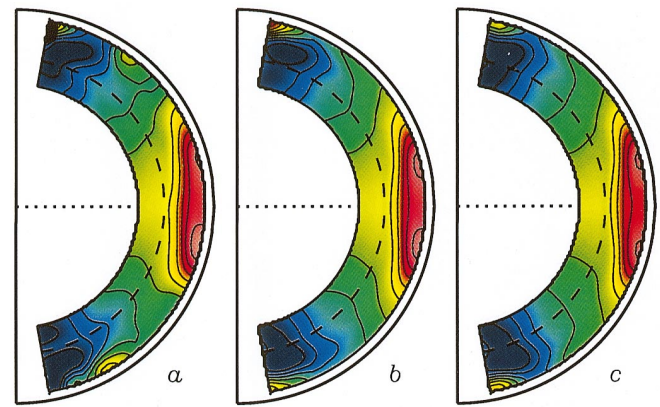


FIG. 10.—Shown are (a) an instantaneous snapshot, (b) a one-rotation-period average, and (c) a ten-rotation-period average of the angular velocity in case LAM (averaged over longitude). The color table and contour levels are the same as those used for the simulations in Fig. 9b–9d.

of angular momentum by banana modes that tend to spin down higher latitudes as described by Gilman (1979), although this process is most efficient for deeper shells. As discussed toward the end of this section, a retrograde thermal wind associated with relatively warm poles may also help to suppress the polar vortex in case LAM. Conversely, the presence of a polar vortex in case TUR can be attributed primarily to the absence of persistent, large-scale banana modes and warm poles. Another process that contributes is the equatorward transport of anticyclonic vorticity in the overshoot region by penetrating downward plumes, which implies a poleward transport of angular momentum (see § 7 and Paper II).

Although the simulated angular velocity profiles both exhibit more cylindrical alignment than the helioseismic inversions shown in Figure 9a, some departures from a Taylor-Proudman state are present. Midlatitude radial angular velocity gradients are generally small, and at low latitudes, case TUR exhibits slightly concave contours and a prograde local maximum in the rotation rate near the bottom of the convection zone.

A more detailed comparison between the differential rotation in the two simulations and that inferred from helioseismology is shown in Figure 11. Figure 11a demonstrates that the amplitude and latitudinal profile of the zonal velocity at the top of the computational domain is similar to that inferred for the Sun from GONG data, apart from a somewhat faster rotation at high latitudes, larger midlatitude gradients, and a weak local minimum at the equator. Note also the equatorial asymmetry in the more turbulent solution, case TUR, even though this profile has been averaged over 10 rotation periods. As mentioned above, the GONG inversions are equatorially symmetric by construction.

The zonal velocity at the top of the computational domain appears very similar in both simulations, although case TUR exhibits less equatorial symmetry and possesses somewhat slower rotation at the midlatitudes and somewhat faster rotation near the poles, as discussed above. Since the angular momentum in the shell is conserved because of the stress-free boundary conditions, this implies a redistribution of angular momentum from midlatitudes to the poles. The retrograde minimum in the zonal velocity at the top of the computational domain occurs at roughly $\pm 50^\circ$ in case TUR compared with $\pm 65^\circ$ in case LAM.

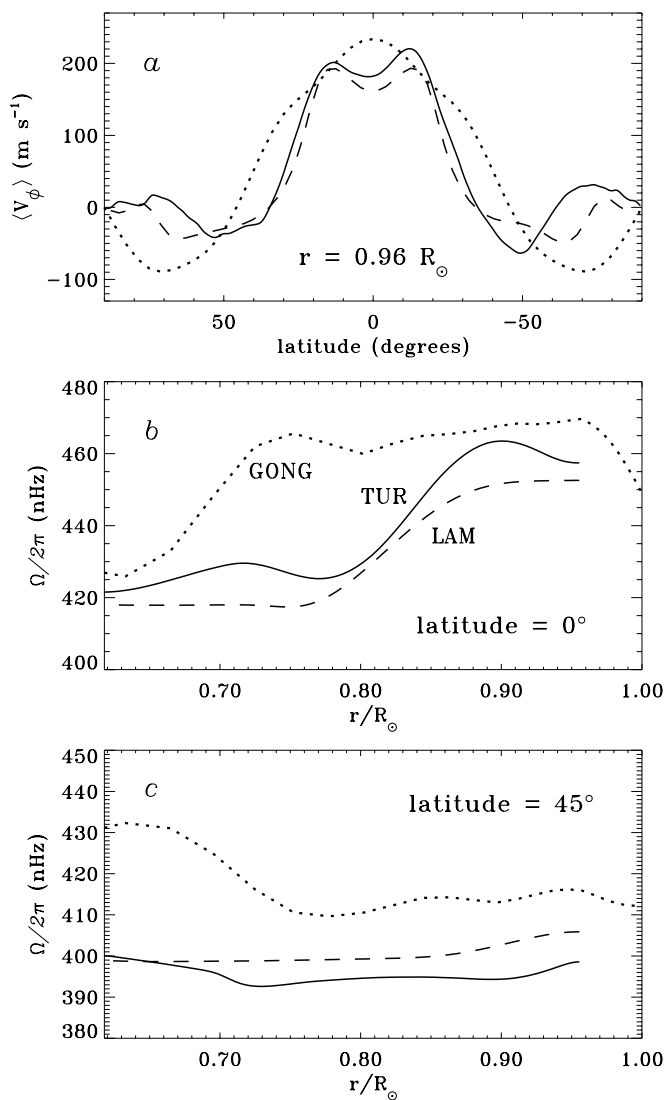


FIG. 11.—Further comparisons between the solar rotation according to helioseismic inversions of GONG data (dotted lines, provided by M. J. Thompson) and the mean rotation profiles in simulations TUR (solid lines) and LAM (dashed lines). (a) the linear zonal velocity with respect to the rotating coordinate system (rotation period = 28 days) as a function of latitude at the outer boundary of the computational domain, $r = 0.96 R_\odot$; (b) the angular velocity as a function of radius at the equator; (c) the angular velocity as a function of radius averaged over latitudes of 45° and -45° . The rotation profiles used are the same as those shown in Fig. 9a, Fig. 9d, and Fig. 10c. Note that the base of the convection zone in the Sun, at $\approx 0.70 R_\odot$ is deeper than that in the models, where $r_b \approx 0.75 R_\odot$.

Toward the base of the convection zone (not shown), the difference is larger, with retrograde minima occurring at roughly $\pm 40^\circ$ and $\pm 70^\circ$ in cases TUR and LAM, respectively.

The radial differential rotation profiles shown in Figures 11b and 11c demonstrate further that there has indeed been a redistribution of angular momentum in case TUR relative to case LAM, although perhaps not as much as one might expect. The rotation is somewhat faster at low latitudes and somewhat slower at midlatitudes, particularly in the upper convection zone and overshoot region. It will be demonstrated in Paper II that this angular momentum redistribution originates from a qualitative change in the way the differential rotation is maintained by nonlinear Reynolds

stresses. In case LAM, the systematic tilting of large-scale, persistent, laminar convection cells by Coriolis forces yields velocity correlations that maintain the differential rotation against diffusion. In contrast, in case TUR, the nonlinear angular momentum transport is dominated by vorticity advection in strong downflow lanes and plumes and diffusion plays a smaller role (see also § 7).

As mentioned above, radial angular velocity gradients at midlatitudes are small throughout the convection zone in both simulations, an encouraging result in light of the helioseismic results (see Fig. 11c). The angular velocity in both simulations is somewhat slower than that given by the GONG inversions, but this can be attributed to the rotation rate chosen for the coordinate system, which is a free parameter ($\Omega/2\pi = 414$ nHz). Since the boundaries in the simulations are stress-free, the specified value fixes the total angular momentum present in the shell. Adopting a slightly larger value for Ω would therefore shift the curves in Figures 11b and 11c upward, in better agreement with the solar rotation (although this would also shift the curves in Fig. 11a upward). Note also that the base of the convection zone in the simulations ($0.75 R_\odot$) is shallower than that in the Sun ($0.70 R_\odot$), and the transition to slower rotation in the underlying stable zone is also shifted upward. Better agreement could likely be obtained with a deeper convection zone in the simulations.

Several other discrepancies between the simulation and helioseismic results still remain. First, the simulations do not exhibit narrow shear layers near the top and bottom of the convection zone comparable to those in the helioseismic inversions discussed at the beginning of this section. As argued there, the upper shear layer is likely associated with supergranular convection in the surface layers that is not captured by our model. The shear layer itself lies outside our computational domain (see Fig. 11b). The absence in the simulations of a tachocline near the base of the convection zone probably implies that our flows are still too diffusive. The formation of such a shear layer may be possible only in higher Reynolds-number flow regimes and may also require a steeper, more solar-like subadiabatic stratification in the radiative interior (see § 3) and/or magnetic effects that are not included in our model (Gilman & Fox 1997; Gough & McIntyre 1998).

Another difference between the simulation and helioseismic results is the polar vortex in case TUR discussed above. Helioseismic inversions and Doppler measurements of the surface rotation show little evidence for such a high-latitude increase in angular velocity. Although such empirical determinations are least reliable near the poles and the corresponding linear velocities are actually relatively small ($\approx 10 \text{ m s}^{-1}$), such a speedup still should have been detected if it were present in the Sun.

It was mentioned at the beginning of this section that a latitudinal entropy variation could help to break the Taylor-Proudman tendency for cylindrically aligned angular velocity profiles. If the variation is such that the polar regions are relatively warm, it could also tend to suppress the formation of a polar vortex by driving a retrograde thermal wind. Zonally averaged entropy profiles for each simulation are shown in Figure 12.

As with the angular velocity, small-scale fluctuations are present in the snapshot for case TUR that largely average out in the ten-rotation mean, although some equatorial asymmetry remains. The large-scale structure indicates a

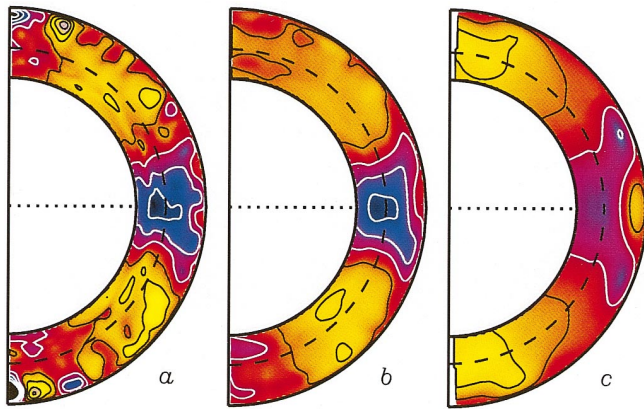


FIG. 12.—Zonally averaged specific entropy perturbations are shown for (a) at one instant for case TUR; (b) averaged over 10 rotation periods for case TUR; and (c) averaged over six rotation periods for case LAM. The color table is similar to that used for the radial velocity and temperature perturbations in Figs. 2 and 3. Black and white contours correspond, respectively, to positive and negative perturbations relative to the spherically symmetric mean (\bar{S}), and contour levels indicate S/C_p values ranging from -7×10^{-7} to 7×10^{-7} , in steps of 2×10^{-7} . Note that the computational domain extends only to $0.96 R_\odot$, although the display is slightly different than in Figs. 9 and 10.

sharp entropy minimum near the equator. This is, in part, yet another manifestation of strong, plumelike downflows, which efficiently transport low-entropy fluid toward the equator in the overshoot region (see Fig. 21). In the upper convection zone, weak entropy maxima occur near the equator and near the poles, although all such variations vanish at the upper boundary because of the fixed-entropy upper boundary condition ($S = 0$).

The mean entropy profile in case LAM (see Fig. 12c) is more equatorially symmetric, and temporal variations (not shown) are relatively small. The entropy maxima at the poles are much more pronounced, as is the low-latitude local maximum in the upper convection zone. This case also exhibits an entropy minimum at the equator in the lower convection zone, but it is less pronounced and broader in latitude. There is generally more radial and latitudinal variation than in case TUR, where the convection is more efficient and more homogeneous.

Relative perturbations in the other thermodynamic variables are comparable in magnitude to S/C_p , as required by the linearized equation of state (4). Thus, the entropy variations in Figure 12 correspond to temperature variations of 1–2 K, as illustrated in Figure 13.

The relatively warm poles in simulation LAM are apparent in Figure 13. At lower latitudes, the two simulations exhibit similar variations in surface temperature, with a maximum near the equator and minima at about $\pm 35^\circ$. The amplitude and midlatitude minima of these variations are suggestive of the solar surface temperature measurements by Kuhn, Libbrecht, & Dicke (1988) and Kuhn & Libbrecht (1991). However, the simulations show no indication of the local minimum at the equator reported in most of the observations, except possibly just after solar minimum.

The local maxima in entropy and temperature near the upper boundary at high and low latitudes are also associated with local maxima in the perturbation density, implying horizontal pressure gradients associated with a meridional circulation.

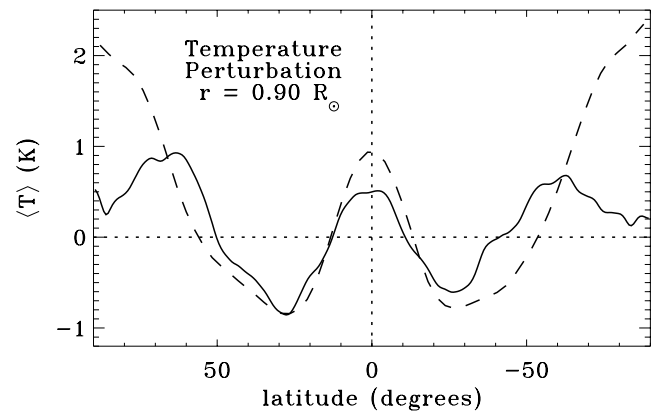


FIG. 13.—Latitudinal variation of the temperature perturbation in the upper convection zone is shown for case TUR (solid line) and case LAM (dashed line). Each curve is averaged over longitude and over one rotation period.

5.2. Meridional Circulation

The axisymmetric meridional circulation in cases TUR and LAM is illustrated in Figures 14 and 15. In both simulations, the circulation at a particular moment in time is very different from a ten-rotation time average. In case TUR, the instantaneous circulation appears very disordered, with much small-scale structure and few discernible large-scale trends. Penetration deep into the stable interior is evident at all latitudes, especially at the poles, where narrow convective rolls extend throughout the convection zone and well into the overshoot region. The more organized appearance of the polar convection is caused largely by the smaller volume involved in the zonal average and becomes less prominent over long temporal means.

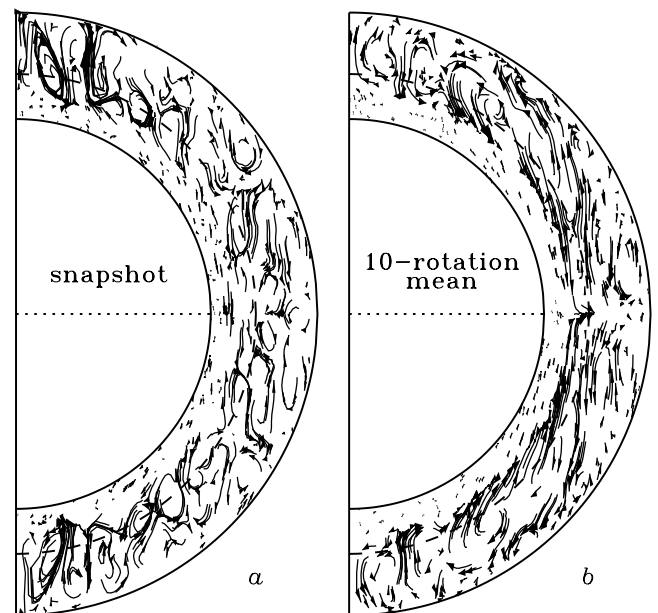


FIG. 14.—Mean circulation in case TUR displayed as the zonally averaged mass flux in the meridional plane, given by $\langle \bar{\rho} v_r \rangle$ and $\langle \bar{\rho} v_\theta \rangle$. Shown are (a) an instantaneous snapshot and (b) an average over 10 rotation periods. Arrows indicate the direction and magnitude of the flow and the dashed line indicates the base of the convection zone.

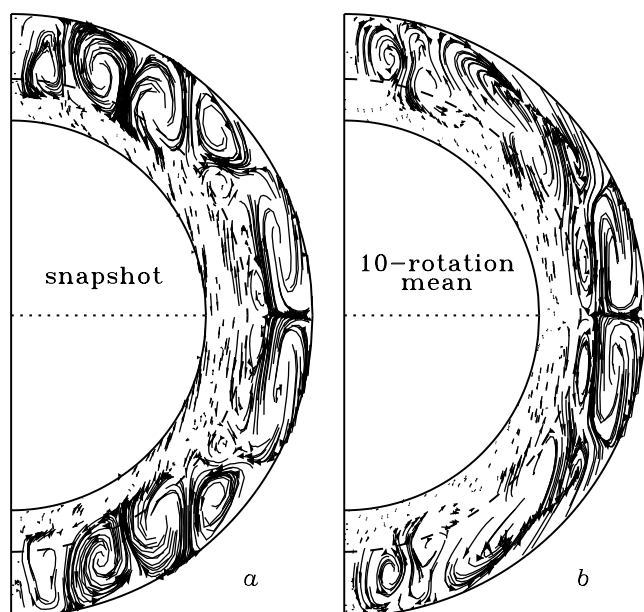


FIG. 15.—Similar to Fig. 14 but for case LAM

The ten-rotation-average circulation in case TUR still exhibits significant residual fluctuations but nevertheless reveals a systematic large-scale flow pattern. The most prominent feature of this pattern is a persistent equatorward circulation in the overshoot region at mid and low latitudes, with a return poleward flow in the mid convection zone. Several weak, layered convection cells are also discernible at low latitudes, with poleward flow near the surface. At high latitudes, the time average reveals several persistent rolls that extend throughout the convection zone and exhibit upward flow at the poles and downward flow at latitudes between $\pm 70^\circ$ – 80° .

The amplitude of the persistent equatorward circulation in the overshoot region is about 4 m s^{-1} , and the poleward flow in the mid convection zone is somewhat faster because of the lower density, about 8 m s^{-1} . The time-averaged circulation at the top of the computational domain ($0.96 R_\odot$) has an amplitude of about 20 m s^{-1} (see Fig. 17). Fluctuations about this mean circulation can be three to five times larger in magnitude, so instantaneous snapshots generally appear very different, as demonstrated in Figure 14.

The circulation in case LAM is much more organized and generally more symmetric about the equator. The instantaneous snapshot (see Fig. 15a) reveals a series of well-defined rolls at high and mid latitudes that have aspect ratios of order unity and which extend throughout the convection zone and penetrate deep into the stable interior. At low latitudes, larger, more latitudinally elongated cells dominate in the upper convection zone, with a weaker counter-circulation at deeper levels. This low-latitude pattern persists in the time average, where the counter-cells in the lower convection zone are more apparent (see Fig. 15b). In contrast, the midlatitude cells do not persist in the time average, which instead reveals a larger scale circulation pattern with poleward flow in the lower convection zone and equatorward flow in the upper convection zone. The time-averaged high-latitude circulation is similar to that in case TUR, with upflow at the poles and downflow at lati-

tudes of about $\pm 80^\circ$, forming cells of aspect ratio about unity that extend from the top of the convection zone into the overshoot region.

The magnitude of the time-averaged circulation in case LAM is comparable to that in case TUR, but slightly larger in the upper convection zone because of the strong low-latitude cells: about 30 m s^{-1} on the surface (see Fig. 17), 10 m s^{-1} in the mid convection zone, and 4 m s^{-1} near the base of the convection zone. Temporal fluctuations are much smaller than in case TUR, but still of order unity with respect to the ten-rotation mean.

The sense of the mean circulation in each simulation can be demonstrated more easily and compared by plotting streamlines of the time-averaged axisymmetric flow. Since the spherical divergence of the zonally averaged mass flux in the meridional plane vanishes according to the anelastic form of the continuity equation (1), we may define a stream function, Ψ , as follows:

$$r \sin \theta \langle \bar{\rho} v_r \rangle = -\frac{1}{r} \frac{\partial \Psi}{\partial \theta}, \quad \text{and} \quad r \sin \theta \langle \bar{\rho} v_\theta \rangle = \frac{\partial \Psi}{\partial r}. \quad (7)$$

Note that this stream function represents the mean mass flux weighted by the moment arm, $r \sin \theta$, so the circulation near the poles is not well represented by Ψ contours. Time-averaged streamlines are shown in Figure 16 for both simulations.

As noted above, the mean circulation in case TUR is dominated by a single cell in each hemisphere, which extends from the equator to latitudes of about $\pm 70^\circ$, with equatorward flow in the overshoot region and poleward flow in the mid convection zone. Above this, there is a thin, oppositely directed counter-cell that produces an equatorward flow at the surface. This counter-cell occupies the upper convection zone at midlatitudes but merges with a stronger, deeper cell at low latitudes. A third layer of cells

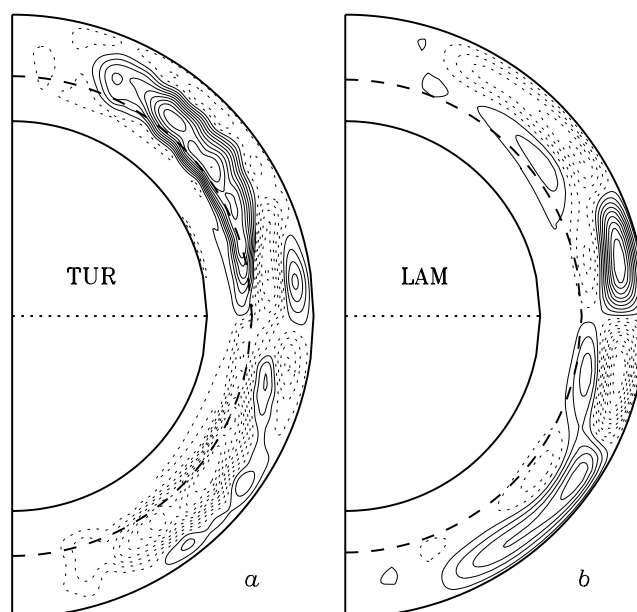


FIG. 16.—Streamlines of the axisymmetric meridional circulation averaged over a ten-rotation-period time interval are shown for (a) case TUR and (b) case LAM. Plotted are contours of the corresponding stream function, defined in eq. (7). Solid lines denote clockwise and dotted lines counterclockwise circulation. The convection zone base in each simulation is indicated by a dashed line.

appears in the upper convection zone at low latitudes, with upflow at the equator.

The mean circulation in case LAM is considerably different. The single large cell that dominates in case TUR is much weaker and smaller, confined to the base of the convection zone at midlatitudes. The midlatitude circulation in the northern (southern) hemisphere is instead dominated by the counterclockwise (clockwise) cell in the upper convection zone, which again merges with a deeper cell at low latitudes. Near the equator, a series of two layered cells in each hemisphere prevails, with the outer pair larger and stronger and producing a poleward surface flow.

The sense and amplitude of the circulation at the top of the computational domain in both simulations is illustrated in Figure 17. In both cases, a poleward surface flow is produced at low latitudes by a pair of cells that occupy the upper convection zone, although the cells are weaker, smaller, and less equatorially symmetric in case TUR. Both simulations exhibit a convergence in the surface circulation at latitudes of about $\pm 20^\circ$ – 30° , above which the flow is equatorward, with an amplitude of about 10 – 25 m s^{-1} . Both simulations also possess an oppositely directed cell near the poles that is strong enough in case LAM to produce another reversal in the surface circulation, appearing as a weak, narrow band of poleward flow at $\pm 70^\circ$ – 80° in latitude.

The sense of the mean latitudinal circulation at the top of the computational domain in our simulations does not agree well with Doppler or helioseismic determinations of the meridional circulation on the solar surface, which suggest poleward flows at all latitudes, with peak magnitudes of about 10 – 20 m s^{-1} (e.g., Hathaway et al. 1996). It is possible that the vigorous, small-scale convection in the solar surface layers drives circulations that are not captured by our model. However, helioseismic results (Giles et al. 1997; Braun & Fan 1998) suggest that the sense of the meridional circulation in the Sun does not change sign down to a depth of at least 30 Mm below the photosphere. Alternatively, improved models achieving more turbulent flow regimes and more realistic upper boundary conditions may produce circulation patterns in which the outer mid-latitude cell seen in Figure 16 is entirely absent.

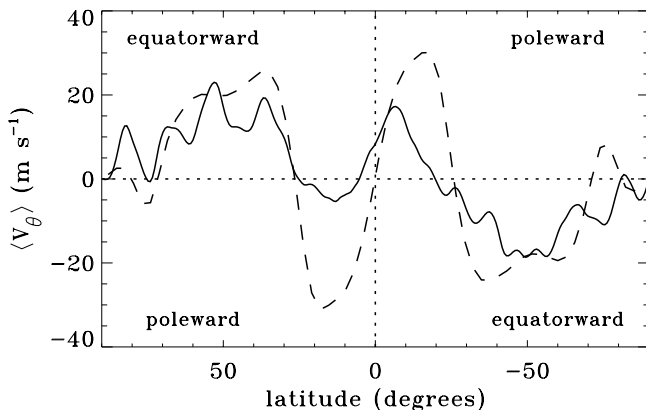


FIG. 17.—Zonally averaged latitudinal circulation at the outer boundary is shown for cases TUR (solid line) and LAM (dashed line), averaged over 10 rotation periods. Positive values indicate southward circulation (toward the equator in the northern hemisphere), and negative values indicate northward circulation.

The axisymmetric circulation is maintained by Coriolis forces acting on the differential rotation, buoyancy forces, Reynolds stresses, and pressure gradients. The kinetic energy in the differential rotation is about 2 orders of magnitude larger than that in the meridional circulation, so even small fluctuations in the differential rotation can produce large variations in the circulation. Large temporal variations in the circulation are also generated by Reynolds stresses from the nonaxisymmetric convection modes, which likewise possess a total kinetic energy about 2 orders of magnitude larger than that in the axisymmetric circulation.

In summary, the meridional circulation is very time dependent, and long time averages are needed to reveal the mean flow patterns, particularly in the more turbulent simulation. The most dramatic difference between cases TUR and LAM is the emergence of a single, large cell in the former solution, with a persistent 4 m s^{-1} equatorward flow in the overshoot region and a return poleward flow in the mid convection zone. The sense of this cell is opposite to the main midlatitude circulation in the convection zone of case LAM. The cell extends all the way to the equator and leads to a sequence of three layered pairs of convection cells at low latitudes, in contrast to the two layered pairs at low latitudes in case LAM.

6. HEAT TRANSPORT AND FLUX BALANCE

In addition to the convective fluxes of enthalpy and kinetic energy, the energy equation (3) includes two types of diffusive heat transport: that caused by radiative diffusion and that caused by unresolved sub-grid-scale turbulence. In a statistically steady state, the radial component of these four fluxes together must account for the full stellar luminosity:

$$F_e + F_k + F_r + F_u = \frac{L_\odot}{4\pi r^2}, \quad (8)$$

where

$$F_e = \bar{\rho} C_p v_r T, \quad (9)$$

$$F_k = \frac{1}{2} \bar{\rho} v_r v^2, \quad (10)$$

$$F_r = -\kappa_r \bar{\rho} C_p \frac{\partial \bar{T}}{\partial r}, \quad (11)$$

and

$$F_u = -\kappa \bar{\rho} \bar{T} \frac{\partial \bar{S}}{\partial r}. \quad (12)$$

These fluxes have been averaged over horizontal surfaces, converted to luminosities, and plotted for both simulations in Figure 18.

In the radiative interior, the flux in both simulations is dominated by radiative diffusion, F_r , but the contribution from this term falls off with increasing radius in the convection zone, where the stellar luminosity is carried primarily by the enthalpy flux associated with the resolved motions, F_e . In the overshoot region, penetrative convection carries low-entropy fluid radially inward, and F_e is negative. This transport is especially efficient in case TUR because of the influence of strong downward plumes, and the reversal in F_e is deeper and more pronounced than in case LAM. In both cases, the inward enthalpy flux in the overshoot region is balanced by a corresponding increase in the radiative flux.

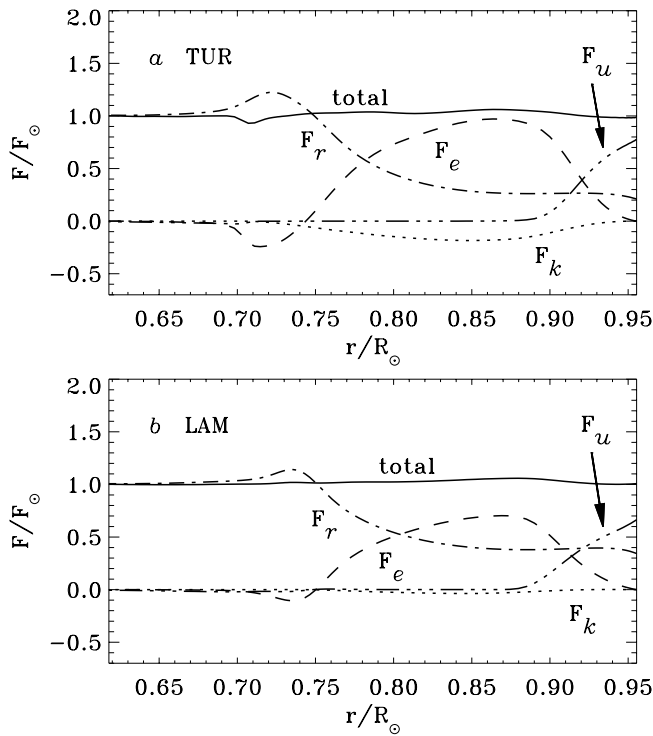


FIG. 18.—Steady-state energy flux balance is illustrated for (a) case TUR and (b) case LAM. As indicated, each plot includes the horizontally averaged luminosity corresponding to the convective enthalpy flux F_e , the convective kinetic energy flux F_k , the radiative flux F_r , and the unresolved eddy flux, F_u , as defined in eqs. (9)–(12). The sum of these four components is shown as a solid line. All curves are normalized with respect to the solar luminosity, $L_\odot = 3.84 \times 10^{33} \text{ ergs s}^{-1}$.

The kinetic energy flux, F_k , is small in case LAM but becomes much more prominent in case TUR, again because of strong downflow lanes and plumes. In both cases, it is radially inward, giving a negative contribution to the total flux balance. A downward kinetic energy flux is a common feature of stratified convection, which is generally characterized by relatively broad, slow upflows and narrower, faster downflows. Both the kinetic energy flux and the radial enthalpy flux caused by the resolved convection vanish at the impenetrable upper boundary, and the

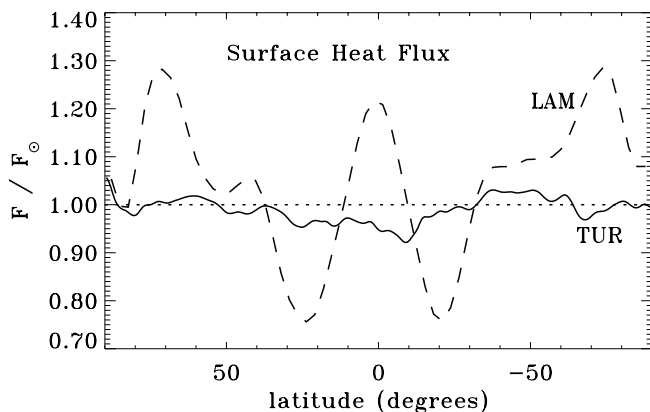


FIG. 19.—Energy flux through the outer boundary, $F_u + F_r$, is shown for case TUR (solid line) and case LAM (dashed line), averaged over longitude and over a time interval of one rotation period.

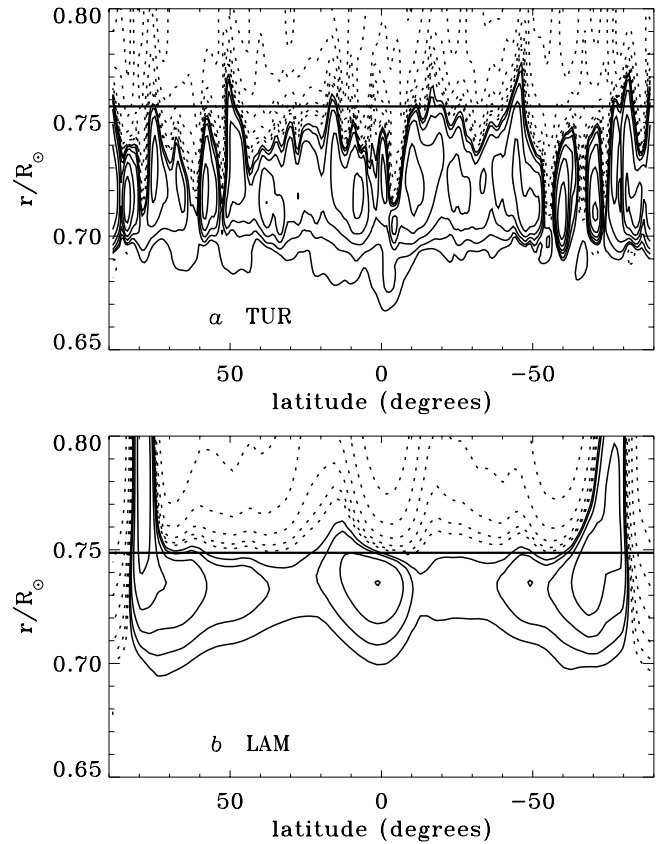


FIG. 20.—Shown are instantaneous snapshots of the zonally averaged convective enthalpy flux, F_e , near the base of the convection zone as a function of latitude and radius for both (a) case TUR and (b) case LAM. Solid contours denote downward flux and dotted contours upward flux. The flux in both panels is normalized with respect to the solar flux, $L_\odot(4\pi r^2)^{-1}$, and contour levels are as follows: $[-0.8, -0.4, -0.2, -0.1, -0.05, -0.025, 0.025, 0.05, 0.1, 0.2, 0.4, 0.8]$. The horizontal solid line in each plot represents the radius at which the corresponding spherically symmetric entropy gradient changes sign.

resulting flux deficit must be carried by the diffusive eddy flux attributed to unresolved turbulence, F_u .

The energy flux flowing through the outer surface is carried solely by the diffusive fluxes F_u and F_r , with the former dominating. Therefore, any latitudinal variations in the emergent surface flux are primarily caused by variations in the radial gradient of the specific entropy perturbations, $\partial S/\partial r$. The latitudinal dependence of the time-averaged surface flux in both simulations is shown in Figure 19.

The emergent flux in case LAM varies by as much as 30%, with maxima at the equator and at high latitudes, about $\pm 75^\circ$. Flux deficits occur at $\pm 20^\circ$ – 30° , corresponding to the persistent axisymmetric downwellings seen in the meridional circulation (§ 5.2). In contrast, the emergent flux in case TUR is more uniform, varying by about 8% with latitude. In this case, there is a flux deficit near the equator that originates from the low-latitude minimum seen in the specific entropy profile (see Fig. 12). Although the latitudinal variations of surface flux in case TUR are smaller than in case LAM, they are still significantly larger than measurements of mean latitudinal irradiance variations in the solar photosphere, which are less than 1% (e.g., Frölich et al. 1991).

The convective enthalpy flux, F_e , can be used to assess how the location of the convection zone base and the extent

of the convective overshoot vary with latitude. As noted above, F_e reverses sign at the base of the convection zone, below which the stratification changes from superadiabatic to subadiabatic and downward quasi-adiabatic fluid motions become warm relative to their surroundings. This downward transport of relatively warm fluid continues until the penetrating motions are decelerated and eventually halted by buoyancy forces and entrainment. Figure 20 exhibits contour plots of the zonally averaged convective enthalpy flux near the base of the convection zone in each simulation. The solid horizontal lines indicate the radius at which the spherically symmetric component of the entropy gradient changes sign, marking the (spherically averaged) interface between the convection zone and the convectively stable interior. Above this level, F_e is directed primarily radially outward (*dotted contours*), but it reverses direction at deeper levels and becomes radially inward (*solid contours*).

Note that the character and extent of this penetration into the stable interior is dramatically different in each simulation. In case TUR, both the level at which F_e reverses sign and the level below which its magnitude becomes negligible exhibit much small-scale latitudinal structure, reflecting the role that intense, localized plumes play in determining both the location of the convection zone base and the extent of the overshoot. This is especially true at high latitudes, where localized features are generally more apparent because of the smaller total volume involved in the zonal average. The larger scale structure indicates somewhat deeper penetration at low latitudes.

In contrast, the enthalpy flux in case LAM is smoother and the overshoot region is narrower. Penetration is deepest near the equator and also at high latitudes, where persistent axisymmetric convection cells (see § 5.2) produce an outward enthalpy flux at the poles and an inward enthalpy flux at latitudes of about $\pm 75^\circ$ – 80° . The enthalpy flux associated with these polar cells shows no sign change near the base of the convection zone, as defined according to the spherically symmetric entropy gradient (*horizontal line*).

7. THE NATURE OF STRONG DOWNFLOWS

It was demonstrated in § 4.1 that strong, intermittent, vortical downflows are a characteristic feature of convection in turbulent parameter regimes, represented here by case TUR. The influence of such downflows is clear not only in the morphology of the convection (see Fig. 2), but also in the nonlinear convective energy transport and the extent,

efficiency, and structure of the convective overshoot (see Figs. 1, 18, and 20). The differential rotation and meridional circulation results discussed in § 5 suggest that strong downflows may also play an important role in establishing and maintaining mean flows, either directly via nonlinear momentum transport through Reynolds stresses or indirectly via changes in the mean entropy profile brought about by convective heat transport. Although a detailed investigation and demonstration of this is reserved for a forthcoming paper (Paper II), here we highlight some of the general characteristics of strong downflows in simulation TUR.

Table 3 lists several mean nonlinear correlations for strong downflows at two different levels in each simulation. Averaging is performed over the northern hemisphere and over a time interval of 10 rotation periods. For the purposes of this table, “strong downflows” are defined as regions in which $v_r \leq -\hat{v}_r$, where \hat{v}_r is the root-mean-square vertical velocity

$$\hat{v}_r = \sqrt{\langle v_r^2 \rangle}. \quad (13)$$

As in Table 3, the angle brackets in equation (13) denote averages over the northern hemisphere and time. The magnitude of \hat{v}_r , in both the mid convection zone and the overshoot region is larger in case TUR than in case LAM, primarily because of faster downflows. The two-dimensional filling factor of strong downflows in Table 3 is approximated by computing the fraction of points on the computational grid at which $v_r \leq -\hat{v}_r$. The results for case TUR range from 14% in the mid convection zone to 9% in the overshoot region, where the downflows becomes more intermittent and plumelike. In contrast, the filling factor in case LAM changes little with depth, remaining at 11%–12% throughout the bulk of the convection zone and overshoot region and thus reflecting the relative invariance of the convection pattern (see § 4.1).

Since $\bar{\rho}$ is independent of θ and ϕ , the first three correlations listed in Table 3 correspond to nonlinear momentum transport, the fourth to kinetic energy transport, and the last to enthalpy transport (cf. eqs. [9] and [10]). The normalization is such that for each of the correlations f ,

$$\frac{\langle f \rangle_d}{|\langle f \rangle|} + \frac{\langle f \rangle_u}{|\langle f \rangle|} = \frac{\langle f \rangle}{|\langle f \rangle|} = \pm 1, \quad (14)$$

where $\langle \rangle_d$ denotes the contribution from regions in which $v_r \leq -\hat{v}_r$ and $\langle \rangle_u$ denotes the contribution from regions in

TABLE 3
STATISTICS OF STRONG DOWNFLOWS^{a,b}

NONLINEAR CORRELATIONS	MID CONVECTION ZONE ($r = 0.84 R_\odot$)		OVERSHOOT REGION ($r = 0.73 R_\odot$)	
	Case TUR	Case LAM	Case TUR	Case LAM
\hat{v}_r	77 m s ⁻¹	47 m s ⁻¹	21 m s ⁻¹	4.1 m s ⁻¹
Filling Factor	0.14	0.12	0.09	0.11
$\langle v_r v_\theta \rangle_d / \langle v_r v_\theta \rangle $	-0.52 (-1)	1.21 (-1)	-0.67 (-1)	0.38 (+1)
$\langle v_r v_\phi \rangle_d / \langle v_r v_\phi \rangle $	-2.95 (-1)	-0.14 (+1)	-0.42 (-1)	0.42 (-1)
$\langle v_\theta v_\phi \rangle_d / \langle v_\theta v_\phi \rangle $	0.06 (+1)	-0.09 (+1)	-5.76 (-1)	0.73 (+1)
$\langle v_r v^2 \rangle_d / \langle v_r v^2 \rangle $	-1.63 (-1)	-2.88 (-1)	-1.86 (-1)	-1.80 (+1)
$\langle v_r T \rangle_d / \langle v_r T \rangle $	0.88 (+1)	0.51 (+1)	-0.41 (-1)	-0.38 (-1)

^a Brackets $\langle \rangle$ denote averages over the northern hemisphere and over a time interval of 10 rotation periods. Subscripted brackets $\langle \rangle_d$ denote contributions to the total from strong downflows alone (see text). “Strong downflows” are defined here as regions in which $v_r \leq -\hat{v}_r$ (see eq. [13]).

^b The symbols in parentheses indicate the normalized value of the total correlation (see text).

which $v_r > -\hat{v}_r$. For each correlation, the relative contribution from strong downflows is listed in Table 3 along with the normalized total, $\langle f \rangle / |\langle f \rangle|$, in parentheses. In case TUR, the total correlations all have the same sign as the strong downflow contribution, implying that strong downflows are responsible for at least part of the net nonlinear energy and momentum transport. This is not true for case LAM, where strong downflows play a less central role and actually oppose some of the net energy and momentum transport that is driven by the remainder of the flow.

Of particular interest in Table 3 are the $v_r v_\phi$ and $v_\theta v_\phi$ correlations, which represent the radial and latitudinal redistribution of zonal momentum (and angular momentum) by nonlinear Reynolds stresses. In the mid convection zone, strong downflows in both simulations tend to conserve their angular momentum, yielding negative $\langle v_r v_\phi \rangle_d$ correlations. These negative correlations in turn imply Reynolds stresses that enhance the downward zonal momentum transport induced by Coriolis forces. In case LAM, this transport in strong downflows opposes the net transport, which is upward (Table 3). In contrast, strong downflows in case TUR are efficient enough to dominate the net zonal momentum transport and redirect it downward.

An even more dramatic difference between the two simulations occurs with the latitudinal transport of zonal momentum in the overshoot region. In case LAM, the nonlinear transport of zonal momentum is toward the equator ($\langle v_\theta v_\phi \rangle_d > 0$), with about 73% of this transport occurring in strong downflow lanes. In contrast, strong downflows in case TUR are associated with an efficient poleward transport of zonal momentum in the overshoot region, which overwhelms the net equatorward transport in upflows and weaker downflows despite its smaller filling factor. This poleward zonal momentum transport is associated with the equatorward advection of anticyclonic vorticity, as discussed later in this section (see Fig. 21).

Also of note in Table 3 is the negative sign of the $v_r v_\theta$ correlation in case TUR, both in the mid convection zone and in the overshoot region. This is in stark contrast to the positive values for case LAM, and it indicates a tilt of downflow lanes toward the rotation axis relative to the vertical. Strong downflows dominate the kinetic energy transport in the mid convection zone in both simulations. Although their relative contribution is greater in case LAM (Table 3), their absolute contribution is greater in case TUR (see Fig. 18). In both simulations, the enthalpy flux is positive in the convection zone and negative in the overshoot region, and strong downflows contribute significantly. However, the relative contribution is somewhat greater in case TUR, where they account for 88% of the total transport in the mid convection zone and 41% in the overshoot region.

The correlations of Table 3, together with the results discussed above in § 4.1 and § 5.2 provide a rough schematic picture of the overall extent and orientation of the strong coherent downflows in simulation TUR. As illustrated in Figure 21, downward plumes at midlatitudes extend through much of the convection zone and are tilted with respect to the vertical toward the rotation axis. A similar tilting of strong, coherent, vortical downflows in high-resolution simulations of turbulent, rotating, compressible convection in Cartesian geometries has been reported by Brummell et al. (1996, 1998). Upon reaching the base of the convection zone, the downflows in case TUR penetrate

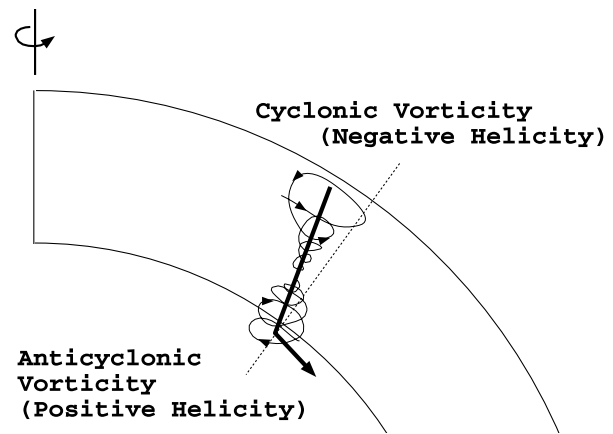


FIG. 21.—Rough schematic diagram of a characteristic, coherent, strong, midlatitude downflow in simulation TUR. Solid lines and arrows illustrate the sense of the flow and the dotted line indicates the radial (vertical) direction for comparison.

deep into the stable interior and are eventually decelerated by buoyancy forces that remove their radial momentum and therefore act to redirect them toward low latitudes, tending to establish an equatorward circulation in the overshoot region as shown in Figures 14 and 16.

As discussed in § 4.1, Coriolis forces in the upper convection zone tend to spin up downflowing fluid parcels that contract because of the density stratification and geometry. The induced cyclonic vorticity implies that the helicity of strong downflows in the bulk of the convection zone is negative in the northern hemisphere and positive in the southern hemisphere. When downflows splash against the stable interior in the overshoot region and diverge, Coriolis forces instead induce anticyclonic vorticity, producing a helicity reversal. This is demonstrated explicitly in Figure 22, which shows the mean helicity in the northern hemisphere as a function of depth for both cases TUR and LAM. Although both simulations exhibit a helicity reversal near the base of the convection zone, the effect is much more pronounced in case TUR because of the influence of strong downflows.

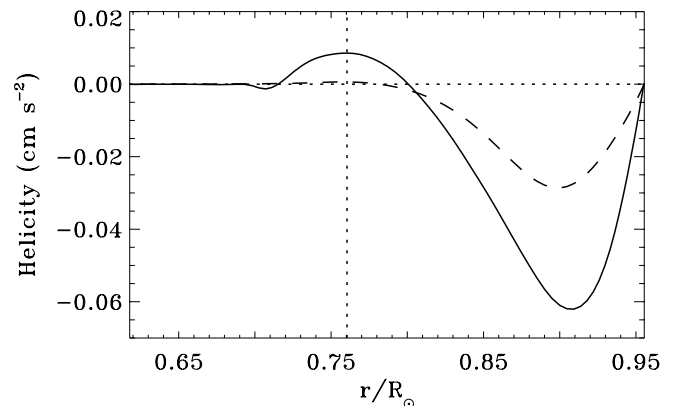


FIG. 22.—Mean helicity is shown as a function of radius, averaged over the northern hemisphere and over a time interval of one rotation period. The solid line represents simulation TUR and the dashed line simulation LAM. The vertical dotted line marks the base of the convection zone for case TUR.

Figure 22 also demonstrates that the magnitude of the helicity throughout the convection zone is larger in case TUR than in case LAM. This can be attributed to both the larger downward velocities attained in the more turbulent solution and the generally more vortical nature of the flow (since the rotation rate of the coordinate system is the same in both simulations, the larger rms vorticity in case TUR is reflected by the larger Rossby number listed in Table 1). The increased vorticity in case TUR arises from the vortex stretching instabilities characteristic of three-dimensional turbulence as well as Coriolis acceleration and entrainment associated with the stronger downflows.

The intense vorticity associated with coherent downflows in case TUR has important implications for the establishment and maintenance of the differential rotation by nonlinear Reynolds stresses. Downward transport of cyclonic vorticity tends to decelerate the rotation in the upper convection zone with respect to deeper levels, which in turn tends to break the cylindrical symmetry and reduce the radial angular velocity gradients established by banana-type convective modes in more laminar simulations. Furthermore, the equatorward transport of anticyclonic vorticity in the overshoot region gives rise to a poleward transport of angular momentum at midlatitudes, which contributes to the polar vortex discussed in § 5.1. These issues will be investigated further in Paper II.

Although the simulations presented in this paper are nonmagnetic, the increased dynamical role of strong, intermittent, downward plumes in turbulent flow regimes has important implications for solar dynamo theory. As mentioned above, overshooting plumes help to establish an extended overshoot region with a nearly adiabatic stratification where magnetic flux could be stored. Furthermore, strong downflows establish a more pronounced helicity reversal and an equatorward circulation in the overshoot region. These results have particular relevance for interface dynamo models (e.g., Parker 1993; Tobias 1997).

8. SUMMARY

By efficiently taking advantage of high-performance, scalably parallel computing platforms, we have extended three-dimensional simulations of global-scale solar convection into turbulent parameter regimes. Our model incorporates a rotating spherical-shell geometry, density stratification under the anelastic approximation, and convective penetration into an underlying stable interior. We have focused primarily on the coupling of convection and rotation, particularly with regard to changes in the convection structure and time-dependence and in the nonlinear transport of energy and momentum as the flows become more turbulent. The motivation is a better understanding of the highly turbulent dynamics occurring in the solar convection zone.

We have presented results from two simulations, similar in every way except for the magnitude of the dissipation. The convection structure in the laminar simulation, case LAM, is dominated by large-scale, regular banana modes at low and mid latitudes, but the more turbulent case TUR exhibits much more small-scale, time-dependent structure, including a more intricate network of downflow lanes in the upper convection zone and a more plumelike downflow distribution in the overshoot region.

The downflow network in the upper convection zone of case TUR includes coherent, latitudinally elongated lanes at low latitudes, but they are not, in general, azimuthally

periodic like the dominant banana modes in case LAM, and they are relatively shorter lived, lasting only days or weeks. The network's horizontal structure is generally more statistically homogeneous than in case LAM, thus producing a more uniform latitudinal distribution of the emergent heat flux at the surface (see Fig. 19). The cellular pattern, particularly at high and mid latitudes, evolves rapidly through the destabilization of downflow interstices and the subsequent creation of new cells by dynamical buoyancy. This process is restricted to relatively turbulent parameter regimes and does not occur in case LAM.

Small-scale fluctuations increasingly dominate the convection structure in case TUR at progressively deeper levels, although some strong, coherent downflows extend from the upper convection zone all the way into the overshoot region, tilted somewhat toward the rotation axis with respect to the vertical (see Fig. 21). Such downflows often originate in the interstices of the downflow network near the surface, but at the base of the convection zone they are generally reduced to localized plumes. They are associated with cooler temperatures and intense vorticity, which is generated by Coriolis forces, vortex stretching, and entrainment. As in previous models (e.g., Yoshimura 1972; Gilman 1983; Glatzmaier 1985a, 1985b), the sense of the Coriolis-induced vorticity is such that the corresponding helicity is negative in the northern hemisphere and positive in the southern hemisphere throughout most of the convection zone but reverses sign near the convection zone base. Although this helicity reversal occurs in both simulations, it is much more prominent in case TUR because of the strong, plumelike downflows.

Strong downward plumes are also responsible for significant differences between the two simulations regarding the structure, extent, and efficiency of convective penetration. In case TUR, they establish a nearly adiabatic stratification in the overshoot region (see Fig. 1) and produce transient, small-scale latitudinal variations in both the base of the convection zone and the penetration depth, as determined by the convective enthalpy flux (see Fig. 20). In contrast, the overshoot in case LAM exhibits a larger scale, banana-type horizontal structure with shallower penetration and a steeper subadiabatic stratification. The penetration in both simulations is somewhat deeper near the equator, and in case LAM it is also relatively deep at high latitudes, where persistent, axisymmetric circulations extend well below the base of the convection zone (see Fig. 15).

The results discussed in § 7 indicate that vorticity and entropy advection in strong, intermittent, coherent downflows contribute substantially to the nonlinear momentum and energy transport in case TUR and, as such, have a profound influence on the mean flows and stratification, as will be demonstrated further in Paper II. This represents an important new result in stark contrast to the situation in more laminar parameter regimes, where systematic, persistent, Coriolis-induced tilts of banana-shaped convective modes dominate the nonlinear momentum transport and maintain the differential rotation (e.g., Gilman 1977; Glatzmaier 1987).

Despite this change in the flow structure and in the nature of the Reynolds stresses, the mean angular velocity profiles are surprisingly similar in the two simulations. In particular, although the more turbulent simulation does resemble the solar rotation profile obtained from helioseismic inversions, it does not represent an obvious

improvement over the laminar simulation. Some cylindrical alignment is still present, the polar rotation rate is too large, and there are no thin shear layers at the top and bottom of the convection zone comparable to those in the helioseismic results. Still, the low-latitude angular velocity contours in case TUR do exhibit a slight concavity in the correct sense, which suggests a promising trend. It is likely that the dissipation in the simulations is still too large to permit turbulent transport processes such as those described by Brummell et al. (1998) to dominate the maintenance of the differential rotation. It is also possible that a thermal wind component may help to break the cylindrical alignment and suppress the tendency for the poles to spin up, thus making the angular velocity profile more solar-like. Although the constant-entropy upper boundary conditions used here tend to suppress this effect, there is some evidence it may be occurring in case LAM. This suggests that a constant-flux upper boundary condition may be more appropriate and may lead to significantly different angular velocity profiles, a conjecture that is supported by further simulations reported in a forthcoming paper (Elliott, Miesch, & Toomre 2000).

Both simulations exhibit axisymmetric circulations in the meridional plane that are relatively weak, with a total kinetic energy only several percent of that in the differential rotation. The zonally averaged meridional circulation, particularly in the turbulent case, is very time-dependent, and long temporal averages are required in order to discern any organized global patterns. In case TUR, time averages reveal a persistent equatorward circulation in the overshoot region of about 4 m s^{-1} , extending from high latitudes all the way to the equator, with a return poleward flow in the mid convection zone (see Fig. 16). Layered countercells in the upper convection zone produce a flow at the top of the computational domain that is poleward at low latitudes and equatorward at high latitudes, with an amplitude of about $10\text{--}20 \text{ m s}^{-1}$. As such, a latitudinal convergence of the surface circulation and an associated downwelling occurs at latitudes of about $\pm 25^\circ$. In case LAM, a mid-latitude convergence still occurs in the circulation at the top of the domain, with poleward and equatorward flow at low and high latitudes, respectively, but the associated cells extend much deeper and, together with relatively weak countercells, yield a circulation pattern in the lower convection zone that is very different from case TUR (see Fig. 16).

The mean axisymmetric circulation near the poles in both simulations is dominated by relatively narrow cells with upflow at the rotation axis, although transient fluctuations can often reverse the sense of the flow.

This paper mainly describes the simulation results, with little discussion of how they come about. A more detailed analysis of the convective momentum and energy transport in these simulations and the maintenance of mean flows will appear in Paper II. In particular, this companion paper will investigate more closely the role of the thermal wind, the influence of viscosity, and the relative contribution to the Reynolds stresses of distinct velocity structures such as banana modes and vortical, localized downward plumes (§ 7).

Helioseismology will provide further information on the structure and time variability of global-scale flows in the solar interior as longer time series of high-quality data become available and as measurement and analysis techniques continue to improve. As such empirical investigations progress, so must theoretical models. Simulations such as those reported here are needed to provide guidance and aid interpretation of helioseismic data, thus contributing to an improved understanding of solar convection.

We thank Nicholas Brummell, John Hart, Mark Rast, and Ellen Zweibel for helpful discussions and Michael Thompson for providing the GONG inversions shown in Figures 9a and 11. Various phases of the simulations were carried out at the Pittsburgh Supercomputing Center (PSC), the National Center for Supercomputing Applications (NCSA), the San Diego Supercomputer Center (SDSC), and the NASA Center for Computational Science (NCCS). Much of the analysis of the extensive data sets was carried out in the Laboratory for Computational Dynamics (LCD) within the Joint Institute for Laboratory Astrophysics (JILA). This work was partially supported by the NSF through grants ECS 92-17394 and ATM 97-31676 and by NASA through grants NAG 5-2256, NAG 5-3077, NAG 5-7996, NAG 5-8133, and NCCS 5-151. Some of the work reported here was carried out while M. S. M. was at NASA Goddard Space Flight Center under support from a National Research Council postdoctoral fellowship and at the University of Cambridge (U.K.) under PPARC support.

REFERENCES

- Antia, H. M., Basu, S., & Chitre, S. M. 1998, *MNRAS*, 298, 543
 Basu, S. 1997, *MNRAS*, 288, 572
 Brandenburg, A., Jennings, R. L., Nordlund, Å., Rieutord, M., Stein, R. F., & Tuominen, I. 1996, *J. Fluid Mech.*, 306, 325
 Braun, D. C., & Fan, Y. 1998, *ApJ*, 508, L105
 Brummell, N. H., Hurlburt, N. E., & Toomre, J. 1996, *ApJ*, 473, 494
 ———. 1998, *ApJ*, 493, 955
 Busse, F. H., & Cuong, P. G. 1977, *Geophys. Astrophys. Fluid Dyn.*, 8, 17
 Cantwell, B. J. 1981, *Annu. Rev. Fluid Mech.*, 13, 457
 Canuto, V. M. 1997, *ApJ*, 482, 827
 Canuto, V. M., & Christensen-Dalsgaard, J. 1998, *Annu. Rev. Fluid Mech.*, 30, 167
 Cattaneo, F., Brummell, N. H., Toomre, J., Malagoli, A., & Hurlburt, N. E. 1991, *ApJ*, 370, 282
 Clune, T. C., Elliott, J. R., Miesch, M. S., & Toomre, J. 1999, *Parallel Computing*, 25, 361
 Corbard, T., Berthomieu, G., Provost, J., & Morel, P. 1998, *A&A*, 330, 1149
 Elliott, J. R. 1997, *A&A*, 327, 1222
 ———. 1998, *A&A*, 334, 703
 Elliott, J. R., Miesch, M. S., Toomre, J., Clune, T. L., & Glatzmaier, G. A. 1999, in *Structure and Dynamics of the Interior of the Sun and Sun-Like Stars*, ed. S. G. Korzennik & A. Wilson (Noordwijk: ESA), vol. 2, 765
 Elliott, J. R., Miesch, M. S., & Toomre, J. 2000, *ApJ*, in press
 Foster, I. T., & Worley, P. H. 1997, *SIAM J. Sci. Stat. Comput.*, 18, 806
 Frölich, C., Foukal, P. V., Hickey, J. R., Hudson, H. S., & Wilson, R. C. 1991, in *The Sun and Time*, ed. C. P. Sonett, M. S. Giampapa & M. S. Matthews (Tucson: Univ. of Arizona), 11
 Germano, M., Piomelli, U., Moin, P., & Cabot, W. H. 1991, *Phys. Fluids A*, 3, 1760
 Giles, P. M., Duvall, T. L., Scherrer, P. H., & Bogart, R. S. 1997, *Nature*, 390, 52
 Gilman, P. A. 1975, *J. Atmos. Sci.*, 32, 1331
 ———. 1977, *Geophys. Astrophys. Fluid Dyn.*, 8, 93
 ———. 1979, *ApJ*, 231, 284
 ———. 1983, *ApJS*, 53, 243
 Gilman, P. A., & Fox, P. A. 1997, *ApJ*, 484, 439
 Gilman, P. A., & Glatzmaier, G. A. 1981, *ApJS*, 46, 211
 Gilman, P. A., & Miller, J. 1986, *ApJS*, 61, 585
 Glatzmaier, G. A. 1984, *J. Comput. Phys.*, 55, 461
 Glatzmaier, G. A. 1985a, *ApJ*, 291, 300
 ———. 1985b, *Geophys. Astrophys. Fluid Dyn.*, 31, 137
 ———. 1987, in *The Internal Solar Angular Velocity*, ed. B. R. Durney & S. Sofia (Dordrecht: Reidel), 263
 Glatzmaier, G. A., & Gilman, P. A. 1981a, *ApJS*, 45, 381
 ———. 1981b, *ApJS*, 47, 103
 Gough, D. O., & McIntyre, M. E. 1998, *Nature*, 394, 755
 Hathaway, D. H., et al. 1996, *Science*, 272, 1306
 Heslot, F., Castaing, B., & Libchaber, A. 1987, *Phys. Rev. A*, 36, 5870
 Howard, R., & LaBonte, B. J. 1980, *ApJ*, 239, L33

- Jetsu, L., Pohjolainen, S., Pelt, J., & Tuominen, I. 1997, *A&A*, 318, 293
Kadanoff, L. P. 1991, in *New Perspectives in Turbulence*, ed. L. Sirovich (New York: Springer), 263
Kosovichev, A. G. 1996, *ApJ*, 469, L61
Kosovichev, A. G., & Schou, J. 1997, *ApJ*, 482, L207
Kuhn, J. R., & Libbrecht, K. G. 1991, *ApJ*, 381, L35
Kuhn, J. R., Libbrecht, K. G., & Dicke R. H. 1988, *Science*, 242, 908
Lesieur, M. 1990, *Turbulence in Fluids* (Dordrecht: Kluwer)
Lumley, J. L. 1991, in *New Perspectives in Turbulence*, ed. L. Sirovich (New York: Springer), 105
Mason, P. J. 1994, *Q. J. R. Meteorol. Soc.*, 120, 1
Miesch, M. S. 1998, *Turbulence in Stellar and Interstellar Environments*, Ph.D. thesis, University of Colorado
Miesch, M. S., Elliott, J. R., & Toomre, J. 1999, in preparation (Paper II)
Parker, E. N. 1993, *ApJ*, 408, 707
Schou, J., et al. 1998, *ApJ*, 505, 390
Siggia, E. D. 1994, *Annu. Rev. Fluid Mech.*, 26, 137
Soward, A. M. 1977, *Geophys. Astrophys. Fluid Dyn.*, 9, 19
Spiegel, E. A., & Zahn, J.-P. 1992, *A&A*, 265, 106
Stein, R. F., & Nordlund, A. 1998, *ApJ*, 499, 914
Tobias, S. M. 1997, *A&A*, 322, 1007
Thompson, M. J., et al. 1996, *Science*, 272, 1300
Tritton, D. J. 1988, *Physical Fluid Dynamics* (Oxford: Oxford Univ. Press)
Wilson, P. R., Burtonclay, D., & Li, Y. 1996, *ApJ*, 470, 621
Xie, X., & Toomre, J. 1993, *ApJ*, 405, 747
Yoshimura, H. 1972, *ApJ*, 178, 863
Zhang, K.-K. 1994, *J. Fluid Mech.*, 268, 211